

AD-A158 144 MASKING OF LIGHT SCATTERING INFORMATION ON MATRIX ELEMENTS FROM COMPLEX SCATTERING(U) ARIZONA UNIV TUCSON 1/1
W S BICKEL JUL 85 CRDC-CR-85035 DAAK11-82-K-0008

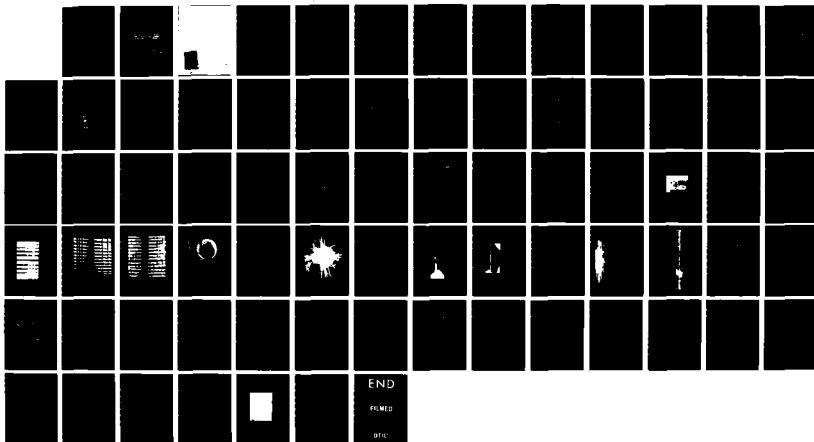
MASKING OF LIGHT SCATTERING INFORMATION ON MATRIX
 ELEMENTS FROM COMPLEX SCATTERING(U) ARIZONAUNIV TUCSON
 W S BICKEL JUL 85 CRDC-CR-85035 DAAK11-82-K-0008

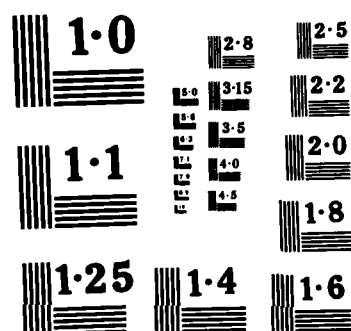
1/1

UNCLASSIFIED

F/G 20/6

NL





NATIONAL BUREAU OF STANDARDS
MICROCOPY RESOLUTION TEST CHART

2

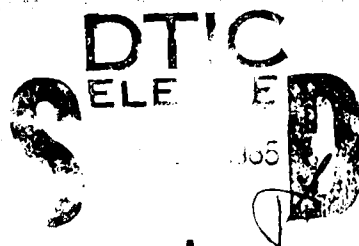
AD-A158 144

CRDC-CR-85035

MASKING OF LIGHT SCATTERING INFORMATION ON MATRIX ELEMENTS FROM COMPLEX SCATTERING

by **William S. Bickel**
UNIVERSITY OF ARIZONA
Tucson, Arizona 85721

DTIC FILE COPY



July 1985

U.S. Army Armament, Munitions & Chemical Command
Aberdeen Proving Ground, Maryland 21010-5423

This document has been approved
for public release and sale in
distribution unlimited.

85 8 20 112

RECEIVED
NATO AREA
DISTRIBUTION
DATE 10/1/54
BY [Signature]
[Signature]
[Signature]

UNCLASSIFIED

SECURITY CLASSIFICATION OF THIS PAGE

REPORT DOCUMENTATION PAGE				
1a. REPORT SECURITY CLASSIFICATION UNCLASSIFIED			1b. RESTRICTIVE MARKINGS	
2a. SECURITY CLASSIFICATION AUTHORITY			3. DISTRIBUTION / AVAILABILITY OF REPORT Approved for public release; distribution unlimited.	
2b. DECLASSIFICATION / DOWNGRADING SCHEDULE				
4. PERFORMING ORGANIZATION REPORT NUMBER(S) CRDC-CR-85035			5. MONITORING ORGANIZATION REPORT NUMBER(S)	
6a. NAME OF PERFORMING ORGANIZATION University of Arizona		6b. OFFICE SYMBOL (if applicable)	7a. NAME OF MONITORING ORGANIZATION	
6c. ADDRESS (City, State, and ZIP Code) Tucson, AZ 85721			7b. ADDRESS (City, State, and ZIP Code)	
8a. NAME OF FUNDING / SPONSORING ORGANIZATION CRDC		8b. OFFICE SYMBOL (if applicable) SMCCR-RSP-B	9. PROCUREMENT INSTRUMENT IDENTIFICATION NUMBER DAAK11-82-K-0008	
8c. ADDRESS (City, State, and ZIP Code) Aberdeen Proving Ground, MD 21010-5423			10. SOURCE OF FUNDING NUMBERS	
			PROGRAM ELEMENT NO.	PROJECT NO.
			TASK NO.	WORK UNIT ACCESSION NO.
11. TITLE (Include Security Classification) Masking of Light Scattering Information on Matrix Elements From Complex Scattering				
12. PERSONAL AUTHOR(S) Bickel, William S.				
13a. TYPE OF REPORT Contractor		13b. TIME COVERED FROM Sep 82 TO Aug 84	14. DATE OF REPORT (Year, Month, Day) 1985 July	15. PAGE COUNT 73
16. SUPPLEMENTARY NOTATION Contracting Officer's Representative: Jerald Bottiger, SMCCR-RSP-B, (301) 671-2395				
17. COSATI CODES			18. SUBJECT TERMS (Continue on reverse if necessary and identify by block number) Light scattering, Mueller matrix, Masking, etc.	
FIELD 20	GROUP 06	SUB-GROUP		
19. ABSTRACT (Continue on reverse if necessary and identify by block number) Changes in light scattering curves due to perturbations on scattering systems are considered, using both measured data and, where possible, computer generated data. It is demonstrated that polydispersivity in size or real refractive index quickly destroys phase information from systems of perfect spheres, while absorption destroys phase information mainly in the backscatter directions and decreases the ratio of backscatter to forward scatter intensity. Several measured Mueller matrices are presented for perfect, bent, rotated, tilted, and surface roughened fibers, and for a highly irregular scatter, road dust. An introductory tutorial on the Mueller matrix description of light scattering is included.				
20. DISTRIBUTION / AVAILABILITY OF ABSTRACT <input checked="" type="checkbox"/> UNCLASSIFIED/UNLIMITED <input type="checkbox"/> SAME AS RPT <input type="checkbox"/> DTIC USERS			21. ABSTRACT SECURITY CLASSIFICATION UNCLASSIFIED	
22a. NAME OF RESPONSIBLE INDIVIDUAL BRENDA C. ECKSTEIN			22b. TELEPHONE (Include Area Code) (301) 671-2914	22c. OFFICE SYMBOL SMCCR-SPS-IR

DD FORM 1473, 84 MAR

83 APR edition may be used until exhausted
All other editions are obsolete

SECURITY CLASSIFICATION OF THIS PAGE

UNCLASSIFIED

PREFACE

The work described in this report was authorized under Contract No. DAAK11-82-K-0008. This work was started in September 1982 and completed in August 1984.

The use of trade names or manufacturer's names in this report does not constitute endorsement of any commercial products. This report may not be cited for purposes of advertisement.

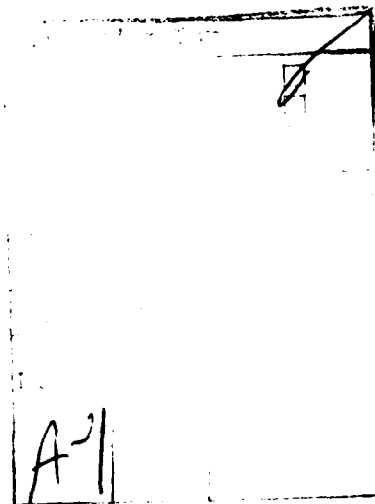
Reproduction of this document in whole or in part is prohibited except with permission of the Commander, US Army Chemical Research and Development Center, ATTN: SMCCR-SPS-IR, Aberdeen Proving Ground, Maryland 21010-5423. However, the Defense Technical Information Center and the National Technical Information Service are authorized to reproduce the document for United States Government purposes.

This report has been approved for release to the public.

Acknowledgments

The following people have contributed to the work reported in this report:

Vince Iafelice	Grad student
David Abromson	Grad student
Yousif Hashim	Grad student
Wilbur Bailey	Grad student
Tim Carone	Grad student
Arleen Watkins	Post Doc
Richard Zito	Research Associate
Joseph Boyer	Visiting Senior Scientist
Gordon Videen	Undergrad
Eric Simms	Undergrad
Joe Simms	Undergrad
Andy Spencer	Undergrad
John Pattison	Undergrad



BLANK

CONTENTS

	Page
1. INTRODUCTION	9
2. RESULTS	12
2.1. Mueller Scattering Matrix Elements for Rayleigh Spheres	12
2.1.1 Introduction	12
2.1.2 Scatterers and the Scattering Matrix	17
2.1.3 The Matrix Element S_{11}	17
2.1.4 The Matrix Element S_{12}	17
2.1.5 The Matrix Element S_{33}	20
2.1.6 The Matrix Element S_{34}	20
2.1.7 All Other Matrix Elements S_{ij}	20
2.1.8 The Light Scattering Matrix for Spheres	20
2.2 The Rayleigh, Rayleigh-Gans and Mie Spheres	22
2.3 Two-Component Sphere Systems, Average Optical Constants and the Masking of S_{ij} Information	25
2.4 Quartz Calibration Fibers	35
2.5 Scattering from Geometrically Perturbed Quartz Fibers	35
2.5.1 Scattering From a Bent Fiber	39
2.5.2 Scattering as a Function of Bend and Rotation.	39
2.5.3 Scattering as a Function of Tilt.	39
2.5.4 Results and Discussion	39
2.5.5 Conclusion	44
2.6 Rough Fiber Scattering	44
2.7 Response of Matrix Elements to Changes in Absorption and Refractive Index	53
2.7.1 Matrix Elements As Probes of Small Perturbations	55
2.7.2 Size, Refractive Index, Absorption, and Wavelength.	55
2.8 Loss of Oscillatory Phase Information on Light Scattering Curves	60
2.8.1 Small Rayleigh Particles	62
2.8.2 Large Mie Spheres	62
2.8.3 Polydispersed Spheres	65
2.8.4 Absorbing Fibers	65
2.8.5 Multiple Scattering Spheres.	65
2.8.6 Irregular Particles	70
3. CONCLUSIONS	73

BLANK

LIST OF FIGURES

<u>Figure</u>		<u>Page</u>
1	Representation of Particles for Light Scattering	11
2	Optical Setup for Polarizer Light Scattering Measurements	13
3	Mueller Matrix Array for Various Input-Output Polarizations	15
4	Mueller Matrix Array of Intensities for Various Input-Output Polarizations	16
5	Measurement of Matrix Element S_{11}	18
6	Measurement of Matrix Element S_{12}	19
7	Measurement of Matrix Element S_{33}	21
8	The Matrix Elements for Small and Large Spheres	23
9	The Matrix Elements for Four Different Sphere Sizes	24
10	Rayleigh-Gans Limit for Large Spheres	26
11	S_{34} Matrix Element at the Rayleigh-Gans Limit	27
12	Average Absorption of a Two-Component Sphere System	29
13	Masking Curves for a Two-Component Sphere System	31
14	The Four Matrix Elements from a Two-Component Sphere System as a Function of Relative Population	33
15	The Four Masking Curves for a Two-Component Sphere System	34
16	Experimental and Theoretical Fits of the Four Matrix Elements from a Calibration Fiber	36
17	Photograph of Mounted Fiber and its Container	37
18	Experimental Setup to Study Bent, Rotated, and Tilted Fibers	38
19	The Variation of Light Scattered from a "Perfect" Fiber as a Function of Rotation Angle θ	40
20	Light Scattering Patterns (S_{11}) as a Function of Fiber Bend	41
21	Light Scattering Patterns (S_{11}) as a Function of Bent Fiber Rotation	42
22	Light Scattering Patterns (S_{11}) as a Function of Fiber Tilt	43
23	Light Scattering Patterns (S_{11}) from a Complex Collection of Random Fibers	45

24	Light Scattering Patterns (S_{11}) from an Apparently Perfect Fiber	47
25	Photomicrograph of a Rough Surface Quartz Fiber	48
26	Matrix Elements of Rough Quartz Fiber of Figure 25	49
27	Light Scattering Out of the Scattering Plane by a Rough Quartz Fiber	50
28	Photomicrograph of a 2.8 Micron Diameter Quartz Fiber Coated With MgO Crystals	51
29	Matrix Elements from an Uncoated and MgO Coated Quartz Fiber	52
30	S_{11} Matrix Elements as a Function of Size, Refractive Index and Absorption	54
31	S_{11} Matrix Elements as a Function of Absorption and Refractive Index	56
32	The Response of Light Scattering Data as a Function of System Perturbation	57
33	Response of Matrix Elements to a Change in Sphere Radius and Illuminating Wavelength	58
34	Response of Matrix Elements to a Change in Refractive Index and Absorption	59
35	Expected Loss of S_{ij} Phase Information as a Function of Particle Irregularity	61
36	Matrix Elements for Rayleigh Spheres	63
37	Matrix Elements for an $r = 0.15$ Micron Sphere and for a Sphere 1 Percent Larger	64
38	Matrix Elements for an $r = 0.6$ Micron Sphere and for a Sphere 1 Percent Larger	66
39	Matrix Elements for a Nine-Component Sphere System	67
40	Matrix Element S_{11} as a Function of Absorption	68
41	Matrix Elements from a Multiple Scattering Sphere System as a Function of Concentration	69
42	Matrix Elements from Arizona Road Dust, a Polydispersed Irregular Particle System	71
43	Electron Micrograph of Arizona Road Dust	72

MASKING OF LIGHT SCATTERING INFORMATION ON MATRIX ELEMENTS FROM COMPLEX SCATTERING

1. INTRODUCTION

There is one overpowering question concerning light scattering as a diagnostic tool: How good is it? For virtually every other diagnostic technique--PIXE, neutron activation, ESCA, x-ray fluorescence, emission spectroscopy, nuclear magnetic resonance (NMR), chemistry, etc.-- the range of sensitivity, specificity, resolution, and discrimination is well-known. Many of these techniques produce signals exactly proportional to the "amount" of a specific parameter over many orders of magnitude. In addition, the signals are often traceable through exact theory to fundamental constants. This makes them valuable as diagnostic tools.

When we began this work no such assessment existed for light scattering data. Perfect systems with known optical constants--refractive index n_1 , absorption n_2 , and size R --are special. They generate light scattering signals exactly predicted by theory which often can be inverted to yield n_1 , n_2 , and R exactly. Studies of such systems can be considered "fundamental research" because all observables can be traced to fundamental optical, electrical, and geometrical constants--refractive indices, permittivities, dielectric constants and radii. However the motivation for such studies soon "runs out of steam" when there seems no need to further test Maxwell's equations, the speed of light, or π .

However, as the perfect systems shift gradually to imperfection (irregularity), theory is driven to approximation and finally to complete fantasy where prediction of even the most complete properties of the scatterer and scattering system are suspect. This situation exists because it is experimentally difficult to get a perfect particle system "with a knob on it" to adjust its parameters in an exactly known way while observing its light scattering signal. Nevertheless, this is where the greatest amount of work needs to be done--how to generate exactly known, imperfect, irregular, and complex systems whose properties are still traceable to fundamental constants. These scatterers belong to the real world.

We found a way to solve this problem. Our system is exactly solvable theoretically, attainable experimentally, and complex--but exactly known. We know that inverted signals do not yield the correct optical constants, but we can find out exactly how close they are. This final report describes some results of our attack on this universally important question.

We are convinced that this research has shed more light on the validity of light scattering as a diagnostic tool than any theoretical approximations or extensive experimental studies of uncharacterized, complex, irregular particles and particle systems.

Our research dealt with the effects of electromagnetic radiation on small particles ($0.01 \text{ micron} < r < 20 \text{ micron}$) of the order of the wavelength of the incident radiation they scatter (0.4416 and 0.6328 micron).

Our approach used the concept of masking where certain properties of light scattering signal can be camouflaged, obscured or completely covered by another. At our disposal are the optical and physical constants n (real refractive index), k (absorption) and r (radius) of perfect spheres and fibers. We also investigate scattering signals from irregular particles and mixtures of perfect particles with exactly known concentrations $N_1, N_2, \dots N_i$. In general, our approach has been to slightly perturb perfect experimental systems exactly described by theory while following the perturbation's effect on the light scattering curve. The more gentle perturbations are reversible and produce linear responses to the light scattering curve, while the more severe ones might be irreversible and produce non-linear responses. In all cases we follow the light scattering response as a function of the perturbation strength to relate a signal to a particle property.

Our approach to the problem is summarized with the help of the three particle axes shown in Figure 1. The most obvious place to start a light scattering study is at the origin which represents a Rayleigh particle. This system can be easily solved exactly on the back of the proverbial envelope. As we move out along the "perfect particle" axis, the sphere systems become more complicated. They become larger, hollow, layered, elliptical and finally rod-like (fibers), but still remain exactly, theoretically solvable. This means that electromagnetic theory, coupled with the well-defined geometrical particle boundaries, and optical constants will exactly predict the light scattering signals (all matrix elements S_{ij} as a function of scattering angle). However, even here, the light scattering signals, when inverted, will not always yield the correct optical constants or be unique.

The inability to solve complex systems is not due to the fact that their boundaries are difficult to define mathematically. This is illustrated by the geometrically perfect particles along the Y axis. A curb can be defined by one geometrical constant as can a sphere. Yet scattering from a curb cannot be solved exactly in the same way that spheres can. The other geometrical particles along the Y axis (pyramids, hexagons, etc.) suffer from the same problem. Here theory is not exact and inversion of light scattering data from such particles would not uniquely describe the particle. Note that particles located on the X-Y plane are even more complicated.

In order to get a particle system "with a knob on it," we developed the particle systems indicated along the Z axis. They are sphere mixtures which are characterized by three very important and useful properties:

- a. they can be solved exactly theoretically
- b. they can be created exactly experimentally
- c. inversion of the data cannot yield the parameters which describe the system

Since light scattered by a system of spheres is simply the sum of the light scattered by each individual sphere, the light scattering signals from such mixtures are exactly predicted. Only when the mixture is a one-component sphere system will the inversion be unique.

We studied such systems to find how effectively certain particles and particle features could be masked or destroyed by the presence of other particles. We determined which matrix elements S_{ij} are sensitive to masked and

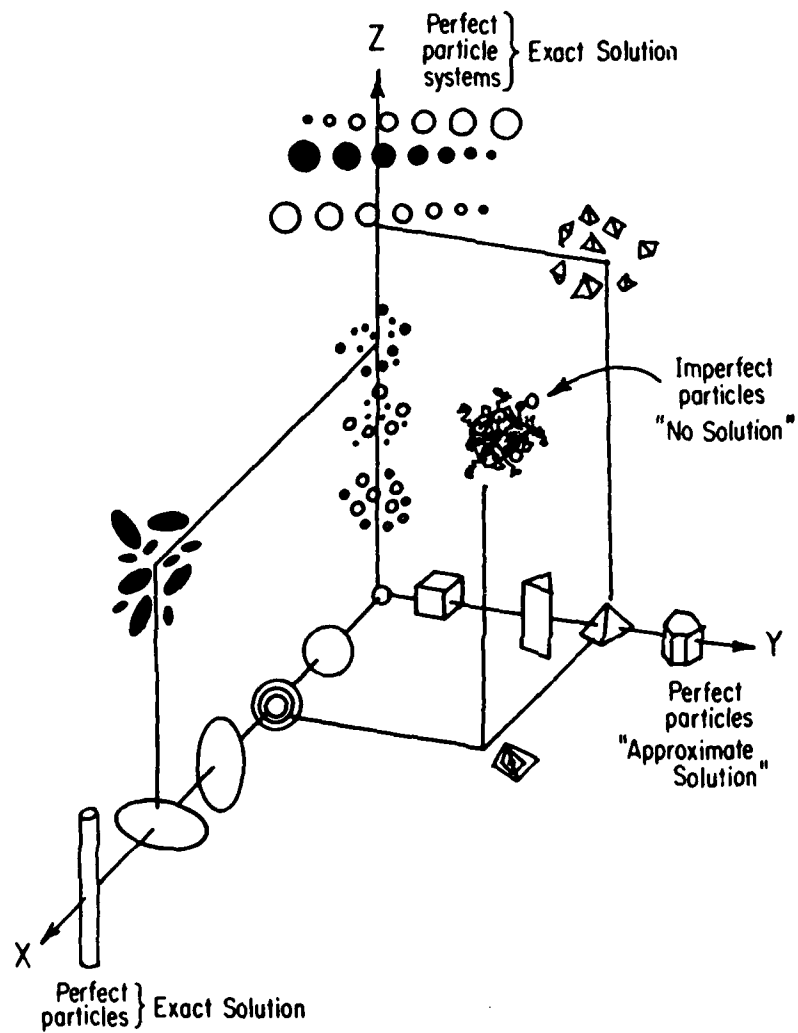


FIGURE 1. Representation of Particles for Light Scattering

The other curves of Figure 9 show the response of the matrix elements as the sphere size decreases to approach the Rayleigh limit. The number of oscillations and their amplitudes decrease as R decreases to $R = 0.30$ (thick solid line) and then to $R = 0.15$ (thin solid line), where the only deviation from the purely symmetric final Rayleigh S_{ij} curve (dotted line) is a small hump in the backscatter region.

Figure 10 shows the matrix elements for the same $R = 0.6$ micron (Mie) sphere particle approaching the Rayleigh-Gans region. Here the refractive index difference between sphere and medium approach zero from $n_1(s) = 1.128$ (ragged line) to $n_1(s) = 1.032$ (thick solid line) and then to $n_1(s) = 1.002$ (thin solid line). In this case, the number of oscillations remain essentially constant (R is constant) while the envelopes of the curves approach the well-known Rayleigh limit. The remaining phase information, which is indicative of particle size at small $n_1(s)$, appears as sharp spikes at well-defined angles.

Matrix element S_{11} is especially interesting. The Rayleigh-Gans limit deviates drastically from the Rayleigh limit which is smooth, symmetric about 90° , and almost constant in intensity. In contrast to the Rayleigh curve, it contains its original phase information whose amplitude now varies by several orders of magnitude. In addition, the backscatter intensity is down by many orders of magnitude compared to the forward scatter.

It is also interesting to observe the behavior of S_{34} at the Rayleigh-Gans limit as the index difference $n_1(s) - n_1(M)$ goes from positive value, through zero to a negative value. At both the Rayleigh and Rayleigh-Gans limit, S_{34} is zero. However it undergoes phase change as it passes through zero, as shown in Figure 11. Here the medium index $n_1(M)$ is 1.000.

The dotted curve is S_{34} for $n_1(s) = 1.004$ with $n_1(s) - n_1(M) = +0.004$.

The solid curve is S_{34} for $n_1(s) = 0.996$ with $n_1(s) - n_1(M) = -0.004$.

Note that the two symmetric cases do not create signals exactly symmetric about the zero polarization axis. This asymmetry persists even as the index difference goes to zero.

The actual Rayleigh-Gans approximation for spheres evokes the condition that the sphere and medium indexes are almost equal but that no reflection occurs at any surface. This approximation preserves, in the limiting case, only the envelopes of the S_{ij} but not the phase information. The S_{ij} signals generated above are the exact signals for Rayleigh and Rayleigh-Gans particles calculated from exact Mie theory. They contain no approximations and therefore carry the phase information into the limit.

2.3 Two-Component Sphere Systems, Average Optical Constants and the Masking of S_{ij} Information.

In this study we examined how the presence of one particle affects the light scattering signal from the other. We still consider independent scattering. When the two components (1) and (2) are identical particles, the light scattering signals from each are identical at all angles. $S_{ij}(1) = S_{ij}(2)$. When the components are different, each particle will scatter but in

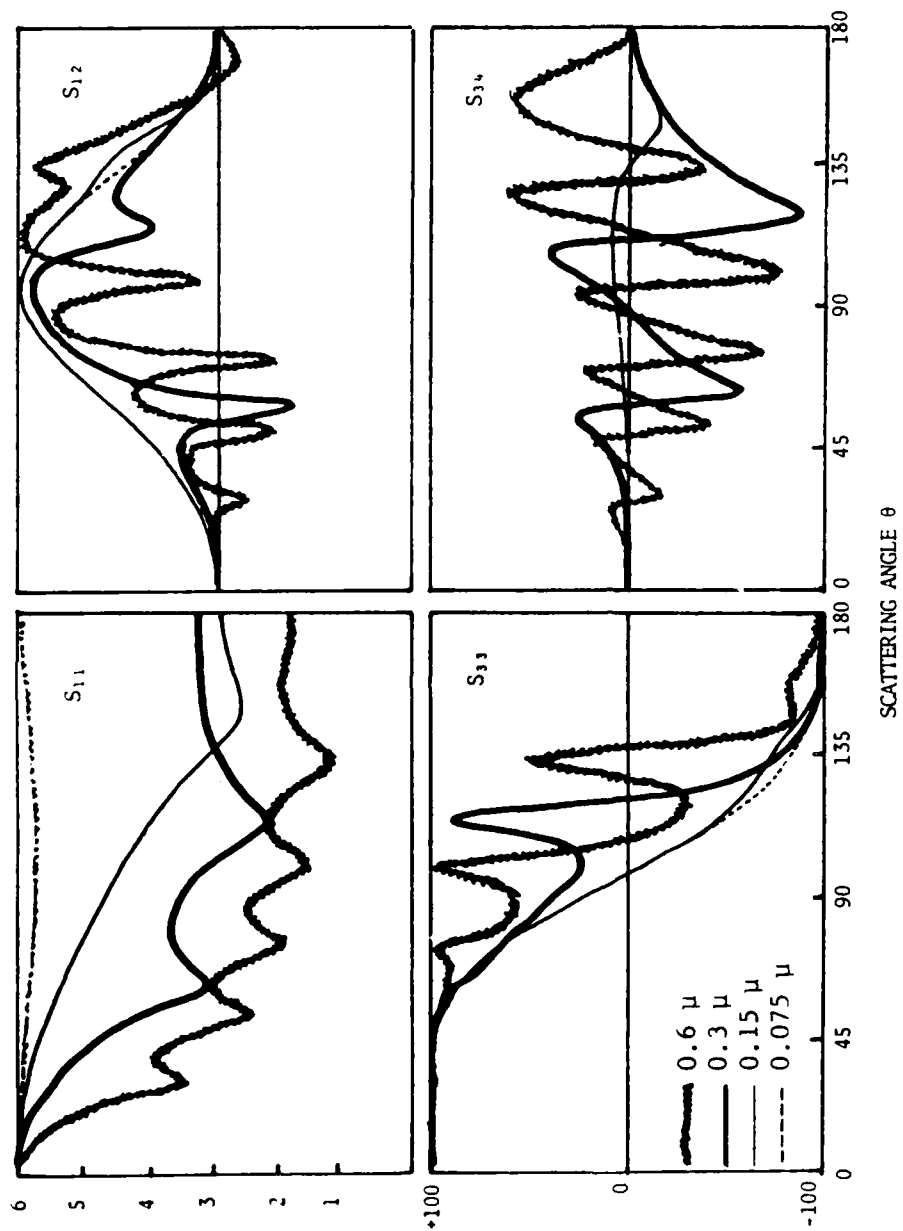


FIGURE 9. The Matrix Elements for Four Different Sphere Sizes

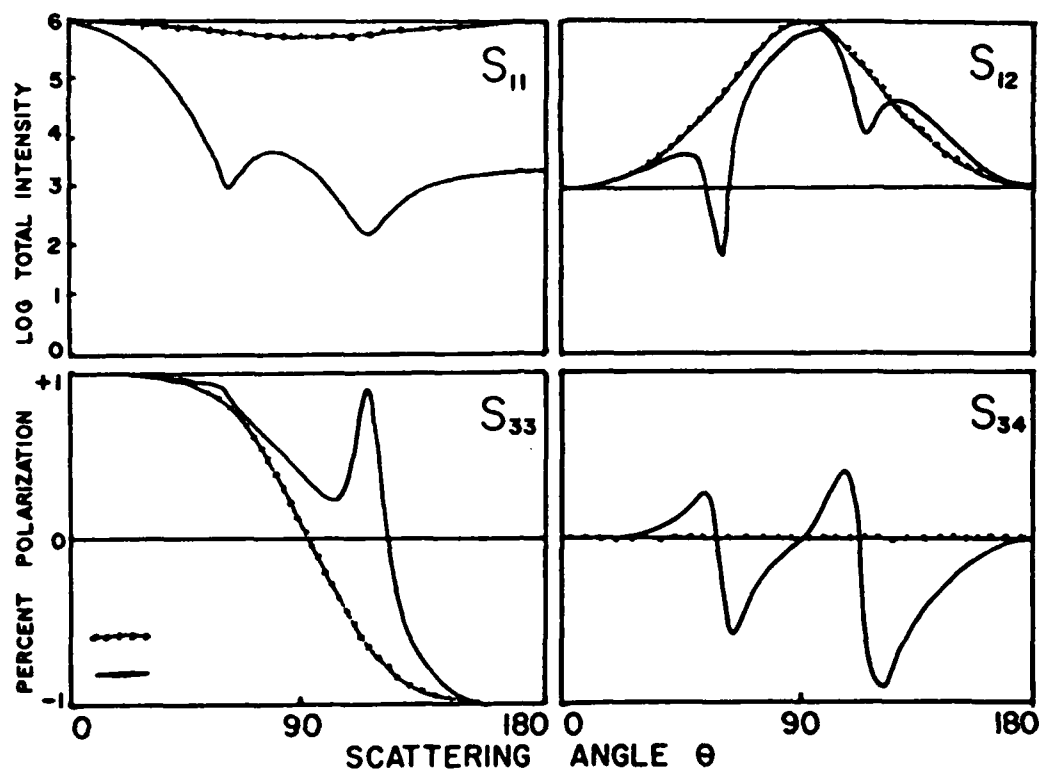


FIGURE 8. The Matrix Elements for Small and Large Spheres

S_{33} , and S_{34} by the total intensity S_{11} . The final curves are summarized by the dotted lines in Figure 8. They represent the "starting point reference curves" for all light scattering curves from particulates. They form the baselines from which curves for larger particles grow and to which curves from complex systems might approach. These curves are independent of particle size, shape, and orientation for individual and collections of Rayleigh particles that scatter single and independently. For non-independent and multiple scattering from even small particles, these curves will appear slightly distorted. It is proper to consider that the Rayleigh curves contain no phase information. Oscillatory phase information, which is truly indicative of larger particles and responsive to particle size changes, appears on these curves only for larger particles. The solid lines of Figure 8 show, for example, the four nonzero matrix elements for larger $r = 0.30$ micron Mie sphere illuminated with 0.4416 micron laser light. It is easy to see how the oscillatory structure developed out of the smooth Rayleigh curves. It is also apparent that the phase information characteristic of larger sphere systems can be destroyed by polydispersivity. Therefore, smooth curves do not imply Rayleigh particle scattering.

2.2 The Rayleigh, Rayleigh-Gans and Mie Spheres.

Mie theory, which predicts sphere scattering exactly for all size spheres, can be approximate in two regions where optical and geometrical constants approach a limiting case.

One region is the Rayleigh region where the size of the particle is considered to be very small compared to the wavelength of the scattered radiation. This approximation permits the small sphere (or any particle) to be treated as an electric dipole. The incident oscillating electric field is essentially constant over the entire particle.

The other is the Rayleigh-Gans region where the sphere can be large but where the refractive indexes of the sphere $n_1(s)$ and that of the surrounding medium $n_1(m)$ are considered to be almost equal so that $n_1(s) - n_1(m) \approx 0$ or $n_1(s)/n_1(m) \approx 1$.

We investigated the response of the matrix elements as a large Mie sphere is extended into the Rayleigh region by letting its radius R go to zero, and into the Rayleigh-Gans region by letting $n_1(s) - n_1(m)$ go to zero.

Rayleigh signals from small particles, which are very common physical scatterers, are well known. Rayleigh scattering is responsible for the blue sky, red sunsets, and other atmospheric phenomena. The Rayleigh-Gans limit is not as common in nature since very few particles have refractive indexes close to air (or vacuum). However, Rayleigh-Gans behavior is extremely important in biology and oceanography where macromolecules, protein, eggs, and cells in water can have indexes very close to that of water. In fact, Rayleigh-Gans phenomena are the reasons why some cells are almost invisible, and sometimes disappear in solutions under microscope or in light scattering experiments.

For a starting point, the jagged lines of Figure 9 are the four nonzero matrix elements for large $R = 0.60$ micron (Mie) sphere with refractive index $n_1(s) = 1.128$, $n_2 = 0.0$, immersed in a medium with $n_1(m) = 1.0$, and illuminated with 0.4416 micron light. These four curves contain the well-known phase information that exactly characterizes the sphere in terms of its optical and geometrical properties.

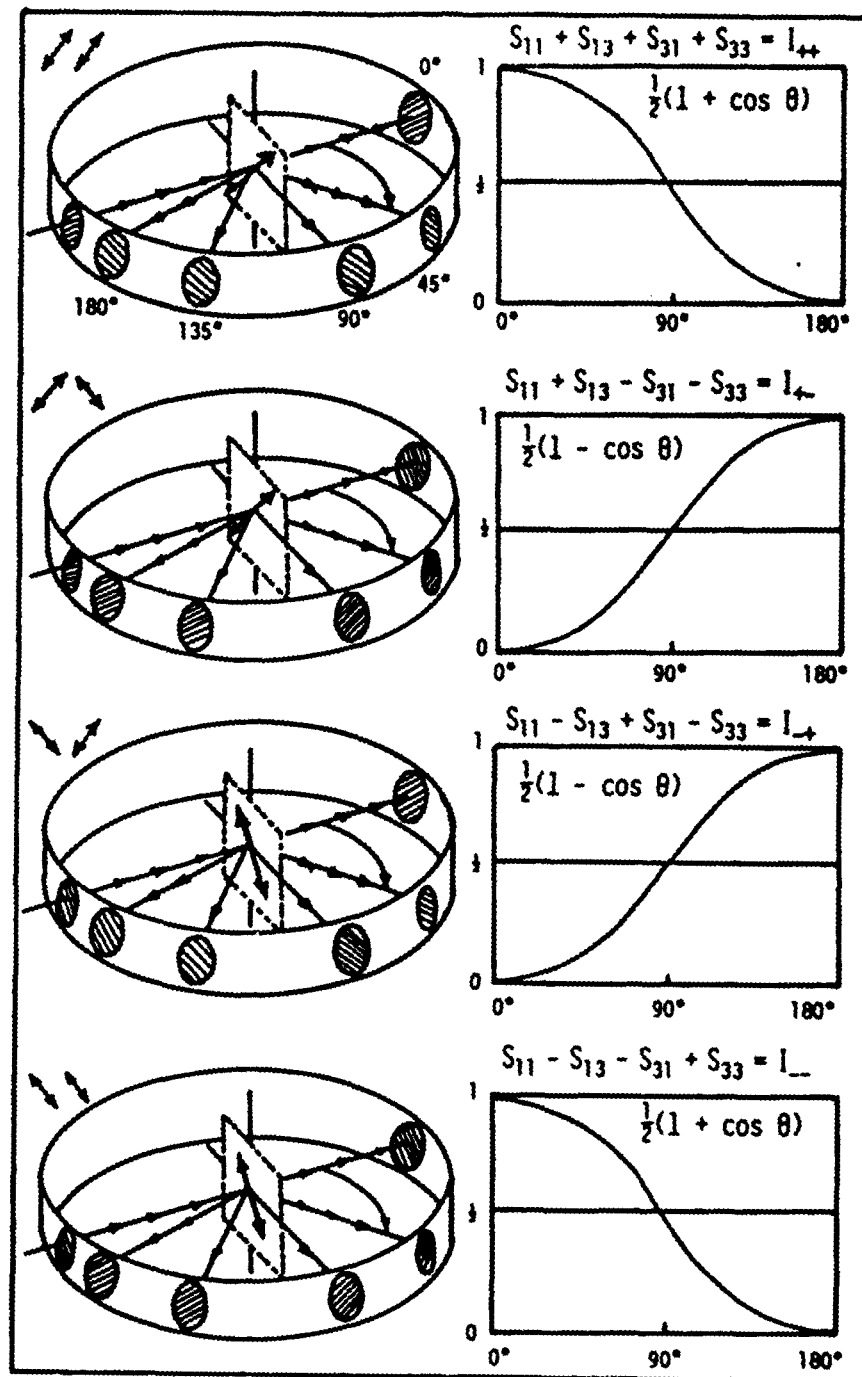


FIGURE 7. Measurement of Matrix Element S_{33}

2.1.5 The Matrix Element S_{33} .

Matrix element S_{33} is determined from four measurements, as indicated in Figures 3 and 4. Figure 7 shows the optical arrangement of the four polarization combinations needed for the measurements described below.

- a. Measure $I(++) = S_{11} + S_{13} + S_{31} + S_{33}$ (+45 goes to +45)
- b. Measure $I(+-) = S_{11} + S_{13} - S_{31} - S_{33}$ (+45 goes to -45)
Then Subtract $I(++) - I(+-) = 2(S_{31} + S_{33})$
- c. Measure $I(-+) = S_{11} - S_{13} + S_{31} - S_{33}$ (-45 goes to +45)
- d. Measure $I(--)= S_{11} - S_{13} - S_{31} + S_{33}$ (-45 goes to -45)

$$\text{Then Subtract } I(-+) - I(--)= 2(S_{31} - S_{33})$$

$$\begin{aligned} \text{Finally, compute } [I(++) - I(+)] - [I(-+) - I(--)] &= \\ [I(++) + I(--)] - [I(-+) + I(+)] &= 4S_{33} \end{aligned}$$

The resultant "intensity" curve for S_{33} therefore varies as $\cos\theta$. This curve is related to the +45 - -45 polarization function for dipole radiation.

2.1.6 The Matrix Element S_{34} .

Matrix element S_{34} , involving circularly polarized light, is determined by the four measurements indicated in Figures 3 and 4. Applying the same procedure described for S_{33} shows that S_{34} for small Rayleigh particles is zero. By definition they are too small to evoke any geometrical or optical path difference between any extreme rays that they scatter. Larger spheres have a nonzero S_{34} matrix element.

2.1.7 All Other Matrix Elements S_{ij} .

All other matrix elements for Rayleigh spheres are either zero or identical to ones just calculated. This can be easily shown by applying the same procedures described above.

2.1.8 The Light Scattering Matrix for Spheres.

We conclude our discussion with some comments about the light scattering matrix for spheres in general, regardless of refractive index and absorption. These comments are valid for individual sphere mixtures and polydispersed systems.

1. For all spheres, $S_{11} = S_{22}$, $S_{12} = S_{21}$, $S_{33} = S_{44}$,
and $S_{34} = -S_{43}$ with all other matrix elements $S_{ij} = 0$.
2. For all spheres, S_{12} and S_{34} are always zero at 0° and 180° . S_{33} is 100% at 0° and -100% at 180° . These bounds hold regardless of how the S_{ij} curve may fluctuate between 0° and 180° .
3. For Rayleigh spheres, S_{11} and S_{12} are symmetric while S_{33} is antisymmetric about $0 = 90^\circ$. S_{34} is zero everywhere.

The four Rayleigh matrix element curves calculated above can be converted directly into the well-known polarization curves by dividing S_{12} ,

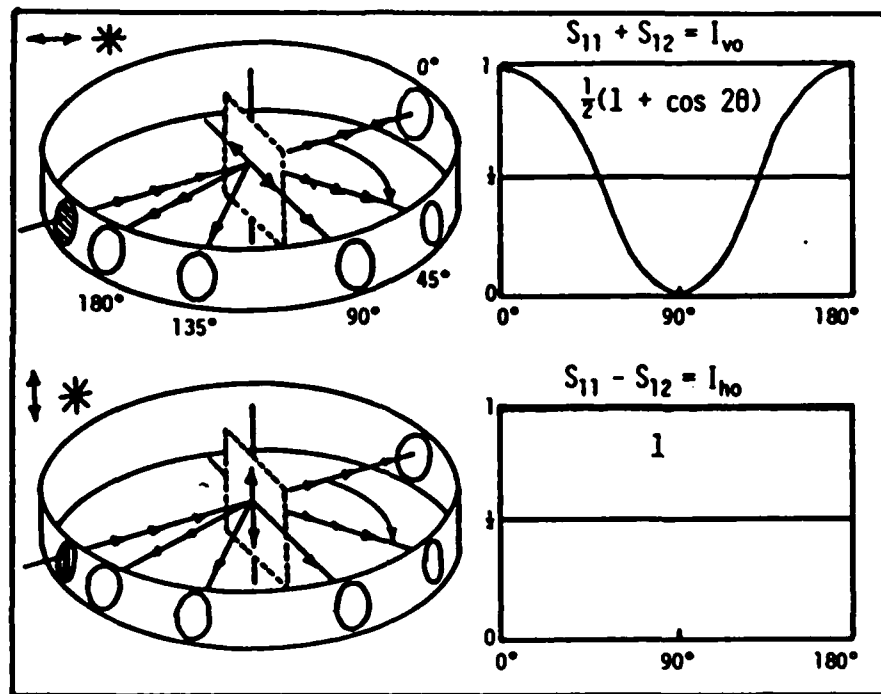


FIGURE 6. Measurement of Matrix Element S_{12}

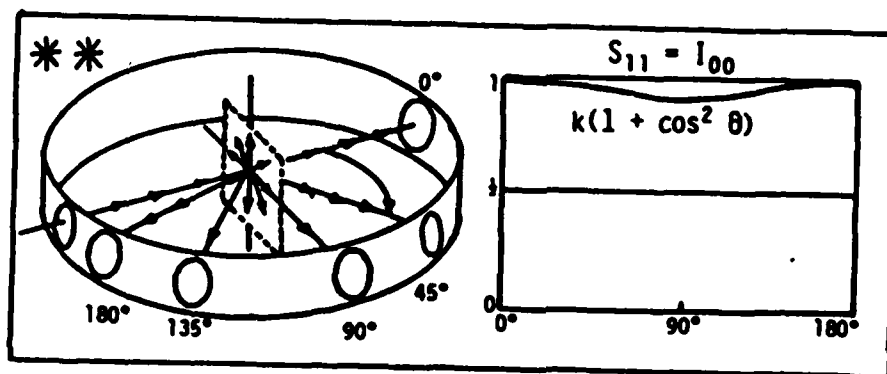


FIGURE 5. Measurement of Matrix Element S_{11}

A previous paper* calculated the functional relationships for the various matrix element sums (intensities) that occur when the "scatterer" is a non-scattering perfect linear polarizer, circular polarizer, or quarter wave plate. These results calibrate the scattering instrument and establish a "frame of reference" for a real scatterer which will behave in part like a linear polarizer, quarter wave plate, circular polarizer, etc., and perhaps like mixtures of them.

2.1.2 Scatterers and the Scattering Matrix.

Scatterers [S] can be divided into three categories: (1) small Rayleigh spheres, (2) large Mie spheres, and (3) polydispersed, nonspherical, irregular, random-oriented particulates. The scattering intensities and polarizations from the first two perfect sphere systems can be calculated exactly from Maxwell's equations and electromagnetic theory. This report shows how to predict the experimentally measured matrix elements for a small Rayleigh sphere using only knowledge about the electric fields and intensity distributions for a driven dipole radiator and the effect of polarizers on the incident and scattered light. This procedure gives insight into the scattering process and demonstrates how polarized intensity measurements are used to calculate matrix elements. The Rayleigh curves are fundamental, easy to calculate, and represent the starting point for studies of larger and irregular particles. The following procedure uses the optical setup of Figure 2 to make the measurements described in Figures 3 and 4.

2.1.3 The Matrix Element S_{11} .

Matrix element S_{11} is determined from the single measurement of the θ -dependent total intensity scattered from a scatterer illuminated with unpolarized light. The exact intensity function for a Rayleigh particle is $I = k(1 + \cos^2\theta)$, which in this special case is independent of frequency. Figure 5 shows how this function would be measured by the optical system shown in Figure 2. Note that as the open hole and detector scan from 0° to 180° , the measured intensity $I(\theta)$, as plotted on a strip chart, will be exactly $I = k(1 + \cos^2\theta)$. The small intensity dip at 90° shows that a small Rayleigh sphere scatters unpolarized light almost isotropically.

2.1.4 The Matrix Element S_{12} .

Matrix element S_{12} is determined from two measurements. The total scattered intensity must be measured for the scatterer, illuminated first with a horizontal and then with a vertical linear polarization. Note from the two optical arrangements shown in Figure 6 that as the open hole and detector are scanned 180° for horizontally polarized illumination, the intensity measured is $I = I(o)1/2(1 + \cos 2\theta) = (S_{11} + S_{12})$. When they are scanned for vertically polarized illumination the intensity is $I = I(v) = (S_{11} - S_{12})$. From Figures 3 and 4 we see that $2 S_{12} = [(S_{11} + S_{12}) - (S_{11} - S_{12})]$, which is the same as $I(v) - I(h)$. The resultant "intensity" curve for S_{12} , therefore varies as $-\sin^2\theta$. This curve is the horizontal-vertical polarization function for dipole radiation.

*Bickel, William S., and Bailey, Wilbur M. Stokes Vectors, Mueller Matrices and Polarized Light Scattering. Unpublished data.

S_{11} * *	S_{12} ↔ *	S_{13} ↗ *	S_{14} ○ *
I_{00}	$I_{H0} - I_{V0}$	$I_{+0} - I_{-0}$	$I_{L0} - I_{R0}$
S_{21} * ↔	S_{22} ↔ ↔	S_{23} ↗ ↔	S_{24} ○ ↔
$I_{0H} - I_{0V}$	$(I_{HH} + I_{VV}) - (I_{VH} + I_{HV})$	$(I_{+H} + I_{-V}) - (I_{-H} + I_{+V})$	$(I_{LH} + I_{RV}) - (I_{RH} + I_{LV})$
S_{31} * ↗	S_{32} ↔ ↗	S_{33} ↗ ↗	S_{34} ○ ↗
$I_{0+} - I_{0-}$	$(I_{H+} + I_{V-}) - (I_{V+} + I_{H-})$	$(I_{++} + I_{--}) - (I_{+-} + I_{-+})$	$(I_{L+} + I_{R-}) - (I_{R+} + I_{L-})$
S_{41} * ○	S_{42} ↔ ○	S_{43} ↗ ○	S_{44} ○ ○
$I_{0L} - I_{0R}$	$(I_{HL} + I_{VR}) - (I_{VL} + I_{HR})$	$(I_{+L} + I_{-R}) - (I_{-L} + I_{+R})$	$(I_{LL} + I_{RR}) - (I_{RL} + I_{LR})$

FIGURE 4. Mueller Matrix Array of Intensities for Various Input-Output Polarizations

s_{11} * * *	s_{12} * * *	s_{13} * * *	s_{14} * * *
s_{21} * * *	s_{22} * * *	s_{23} * * *	s_{24} * * *
s_{31} * * *	s_{32} * * *	s_{33} * * *	s_{34} * * *
s_{41} * * *	s_{42} * * *	s_{43} * * *	s_{44} * * *

FIGURE 3. Mueller Matrix Array for Various Input-Output Polarizations

The following example shows how to determine what scattering matrix elements S_{ij} are involved when a particular set of input-output polarizers are used to prepare and analyze the scattered light. We assume that the arbitrary scatterer $[S]$ is illuminated with horizontally polarized light $|h\rangle$. The scattered Stokes vector will be $|V_s\rangle = [S]|h\rangle$. In terms of the specific Mueller matrices and Stokes vectors involved we have

$$\begin{array}{ccc}
 [S] & * & |h\rangle = |V_s\rangle \\
 \left[\begin{array}{cccc} S_{11} & S_{12} & S_{13} & S_{14} \\ S_{21} & S_{22} & S_{23} & S_{24} \\ S_{31} & S_{32} & S_{33} & S_{34} \\ S_{41} & S_{42} & S_{43} & S_{44} \end{array} \right] & \left[\begin{array}{c} 1 \\ 1 \\ 0 \\ 0 \end{array} \right] & = \left[\begin{array}{c} S_{11} + S_{12} \\ S_{12} + S_{22} \\ S_{13} + S_{32} \\ S_{14} + S_{42} \end{array} \right] \quad (1)
 \end{array}$$

We see that the scatterer $[S]$ mixes the initially pure polarization state $|h\rangle$ to produce a scattered Stokes vector with mixed polarizations. In addition, each Stokes component is now a mixture of two matrix elements. The first component ($S_{11} + S_{12}$) is the total intensity.

If this scattered light is now passed through a +45 linear polarizer $[+]$, we get $[+]|V_s\rangle = |V_f\rangle$, which will be detected by the detector. Specifically we have:

$$\begin{array}{ccc}
 [+] & * & |V_s\rangle = |V_f\rangle \\
 \left[\begin{array}{cccc} 1 & 0 & 1 & 0 \\ 0 & 0 & 0 & 0 \\ 1 & 0 & 1 & 0 \\ 0 & 0 & 0 & 0 \end{array} \right] & \left[\begin{array}{c} S_{11} + S_{12} \\ S_{21} + S_{22} \\ S_{31} + S_{32} \\ S_{41} + S_{42} \end{array} \right] & = \left[\begin{array}{c} S_{11} + S_{12} + S_{31} + S_{32} \\ 0 \\ S_{11} + S_{12} + S_{31} + S_{32} \\ 0 \end{array} \right] \quad (2)
 \end{array}$$

The first component of the final Stokes vector is now a mixture of four matrix elements. The first element sum ($S_{11} + S_{12} + S_{31} + S_{32}$) has special experimental significance since it is the total intensity that will be measured by the detector.

We put the results of all such calculations for all 16 Stokes vector combinations into a final matrix array shown in Figure 3. Each matrix element label S_{ij} is in the uppermost left-hand corner of each matrix element block. The symbols to the immediate right of S_{ij} represent the kind of light involved in the measurement. Symbols below the dotted line in each box show the complementary orientations of the input-output polarizations. The actual matrix element combinations involved in that intensity measurement are given on the right of each symbol pair. Each matrix element sum is the intensity measured using a particular input-output polarization combination. S_{11} is determined with one measurement. The matrix elements of row 1, column 1 need two measurements, while all the others need four. Therefore 49 θ -dependent intensity measurements are needed to uniquely determine the 16 θ -dependent matrix elements which completely characterize the scatterer. They are displayed in Figure 4.

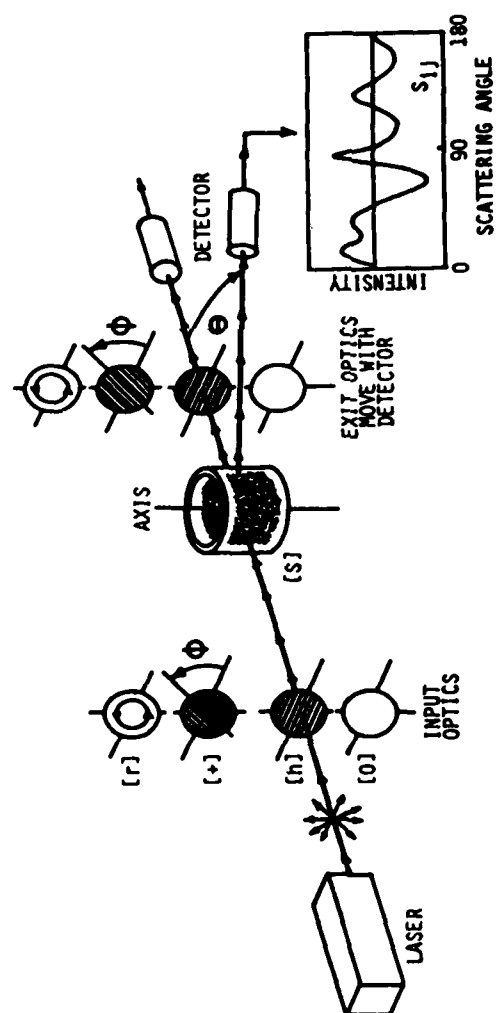


FIGURE 2. Optical Setup for Polarizer Light Scattering Measurements

perturbed features and which ones best yield the correct optical and physical constants. We also applied various analytical techniques to detect the masked particle or particle feature near detection threshold. Such studies can tell how much light scattering information must be gathered to get an accurate description of the scatterers--which matrix elements and what θ -range contain the most useful information.

Our first studies dealt with perfect spheres and fibers for which the errors and uncertainties could be related to fundamental constants. Our later work dealt with the more complex problem of sphere mixtures and finally irregular particles and irregular particle systems. Although the conclusions we draw are often very system-dependent, the techniques we developed can be used to directly assess the accuracy of the optical and physical constants obtained from light scattering data from many real-life systems. Since virtually all light scattering (environmental, biological, astronomical, physical, industrial, etc.) is from non-perfect systems, this approach has special significance, and the results have special value for the analysis of real and natural scatterers.

2.1. Mueller Scattering Matrix Elements for Rayleigh Spheres.

All 16 elements of the Mueller light scattering matrix for a Rayleigh sphere can be predicted from systematic application of the input-output polarizers used to measure scattering intensities from a classical electric dipole. A careful examination of dipole scattering gives good insight into the origin and interpretation of each matrix element.

2.1.1. Introduction.

In a previous paper we described the most general light scattering experiment and derived the general Mueller scattering matrix elements S_{ij} in terms of the input-output Stokes vectors required to characterize the scattering process. A particular light scattering data point is generally nothing more than the value of a particular matrix element measured at a particular angle. Of the infinite number of angles and polarization combinations to choose from, only a small number of highly motivated measurements is needed to completely characterize the scatterer.

The experimental setup that can measure the polarized intensities scattered by the scatterer [S] into the angles θ and ϕ is shown in Figure 2. The input optics can be selected to be: an open hole [0], a horizontal linear polarizer [h], a +45 linear polarizer [+], or right-hand circular polarizer (r). The exit optics choices are the same and can be chosen independently of the input optics. In addition, they can be swung with the detector through the scattering angle θ from 0° to 180° . These choices are sufficient because only three definite Stokes vector components are needed to uniquely establish the polarization states of the beam. They are linear polarization (relative to any axis), a linear polarization at 45° to the first axis, and a left- or right-handed circular polarization. These 3×3 input-output combinations make a set of nine polarization measurements. In addition, the scatterer [S] can be illuminated also with completely unpolarized light (total intensity) and the total intensity output can be measured. Therefore, 16 possible input-output Stokes vector combinations must be measured in order to get the total information about the scatterer.

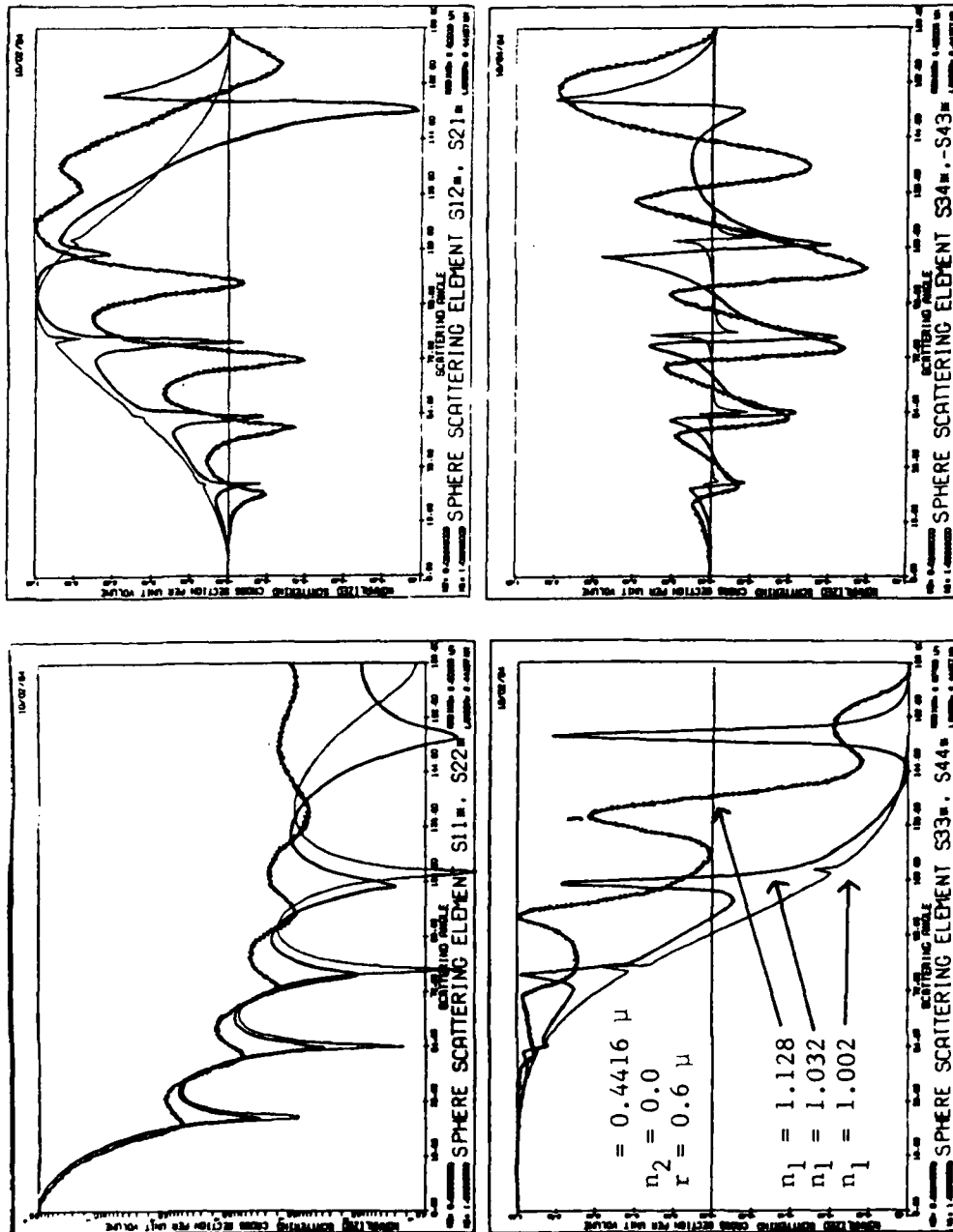


FIGURE 10. Rayleigh-Gans Limit for Large Spheres

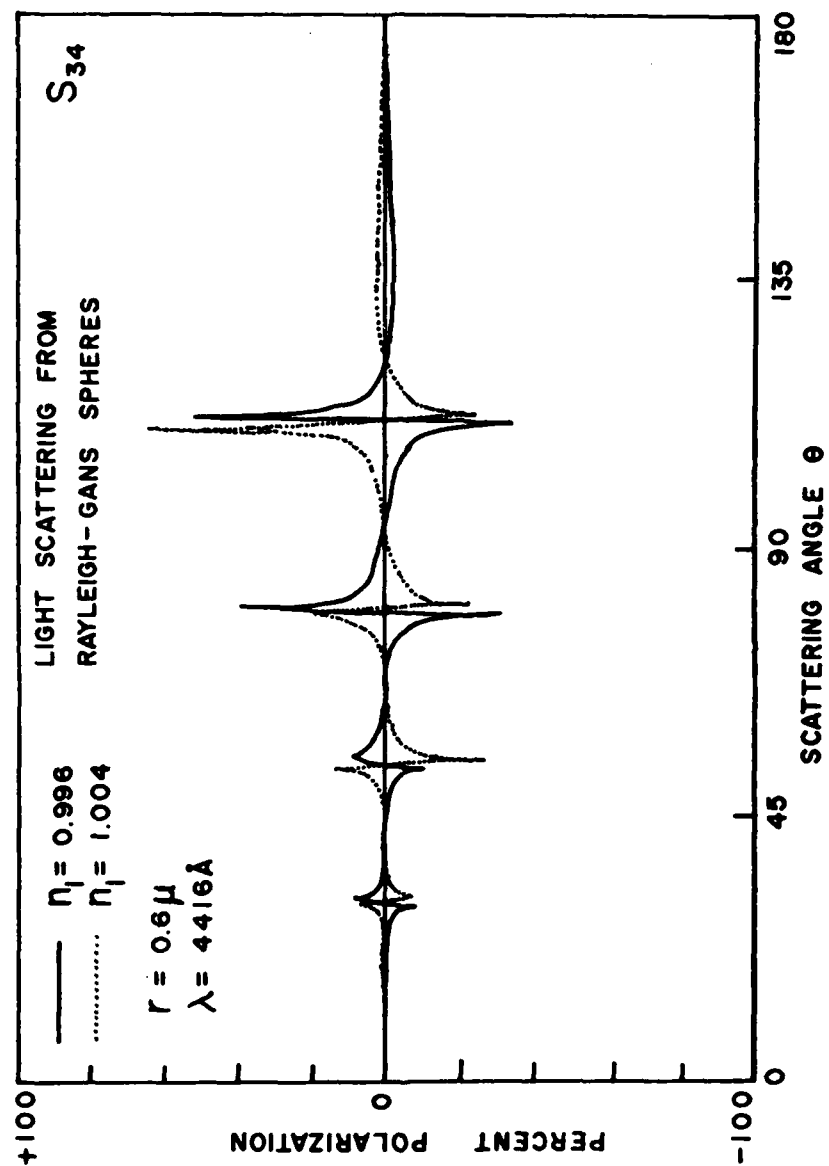


FIGURE 11. S_{34} Matrix Element at the Rayleigh-Gans Limit

competition with the other. The resultant $S_{ij}(1,2)$ will be determined by the intensities scattered by each component at angle θ as well as the degree of polarization at angle θ .

The total intensity $S_{11}(T)$ will simply be the sum $S_{11}(1) + S_{11}(2)$ of the individual intensities. The other $S_{ij}(T)$ for the combination which involves polarizations are not simply the sums but depend on what intensity a particular polarization resides on. The polarization of the particles that scatter more light will dominate the polarization of the mixture. For a two-component system of particles (1) and particles (2) we can write:

$$P_1 = \frac{I_1^l - I_1^r}{I_1^l + I_1^r} \quad P_2 = \frac{I_2^l - I_2^r}{I_2^l + I_2^r} \quad (3)$$

$$P(\Sigma) = \frac{(I_1^l - I_1^r) + (I_2^l - I_2^r)}{(I_1^l + I_1^r) + (I_2^l + I_2^r)} = \frac{P_1(I_1^l + I_1^r) + P_2(I_2^l + I_2^r)}{I_1^T + I_2^T} = \frac{\Delta P_1 I_1}{\Sigma I_1} \quad (4)$$

This shows that if a particle with high polarization does not scatter much light, its contribution to the polarization P of the system will be low. For example, if $P(1) = 100\%$ with $S_{11} = 1$ and $P(2) = 3\%$ with $S_{11} = 300$ the polarization $P(1,2)$ for the system will be only 3.32%, i.e., dominated by the "brighter particle." This kind of normalization is taken into account in all calculations of S_{ij} involving many spheres.

Using these normalization procedures we investigated the role of "average optical constants" for a two- (or more) component system. In our first experiments, we concentrate especially on the concept of average absorption, which is one of the more controversial optical constants for mixtures and complex scattering systems. Figure 12 shows the accuracy to which the four matrix elements are able to predict the average absorption $n_2(av)$ of a two-component sphere system. For this study we chose the following system:

Two-component sphere system (1) and (2)

$R(1) = R(2) = 0.40$ micron
 $N(1) = N(2) =$ total number of spheres
 $n_1(1) = n_1(2) = 1.10$ (the refractive index)
 $n_2(1) = n_2(2) = 0.10$ (the complex part) $n^* = n_1 + in_2$

To generate the S_{11} curve labeled $n_2(av) = 0.05$, we first generate the matrix element curve for the two-component mixture with parameters given above, but specifically with $n_2(1) = 0.00$ and $n_2(2) = 0.10$. The resulting $S_{11}(1,2)$ matrix element curve can be characterized with an average absorption of $n_2(av) = 0.05$. This curve was then compared to single component S_{11} matrix element curves each having definite absorption n_2 which ran from 0.0 to 1.2. For each value of absorption, the absolute difference $S_{11}(n_2av) - S_{11}(n_2) = \Delta$ of the two matrix elements was calculated. For example, as absorption n_2 ran from 0.0 to 1.2, the single S_{11} curve labeled 0.05 was generated. Similar procedures were followed for all other matrix element curves of Figure 12.

In general as n_2 increases, all curves decrease in value to a minimum (not zero) and then increase again.

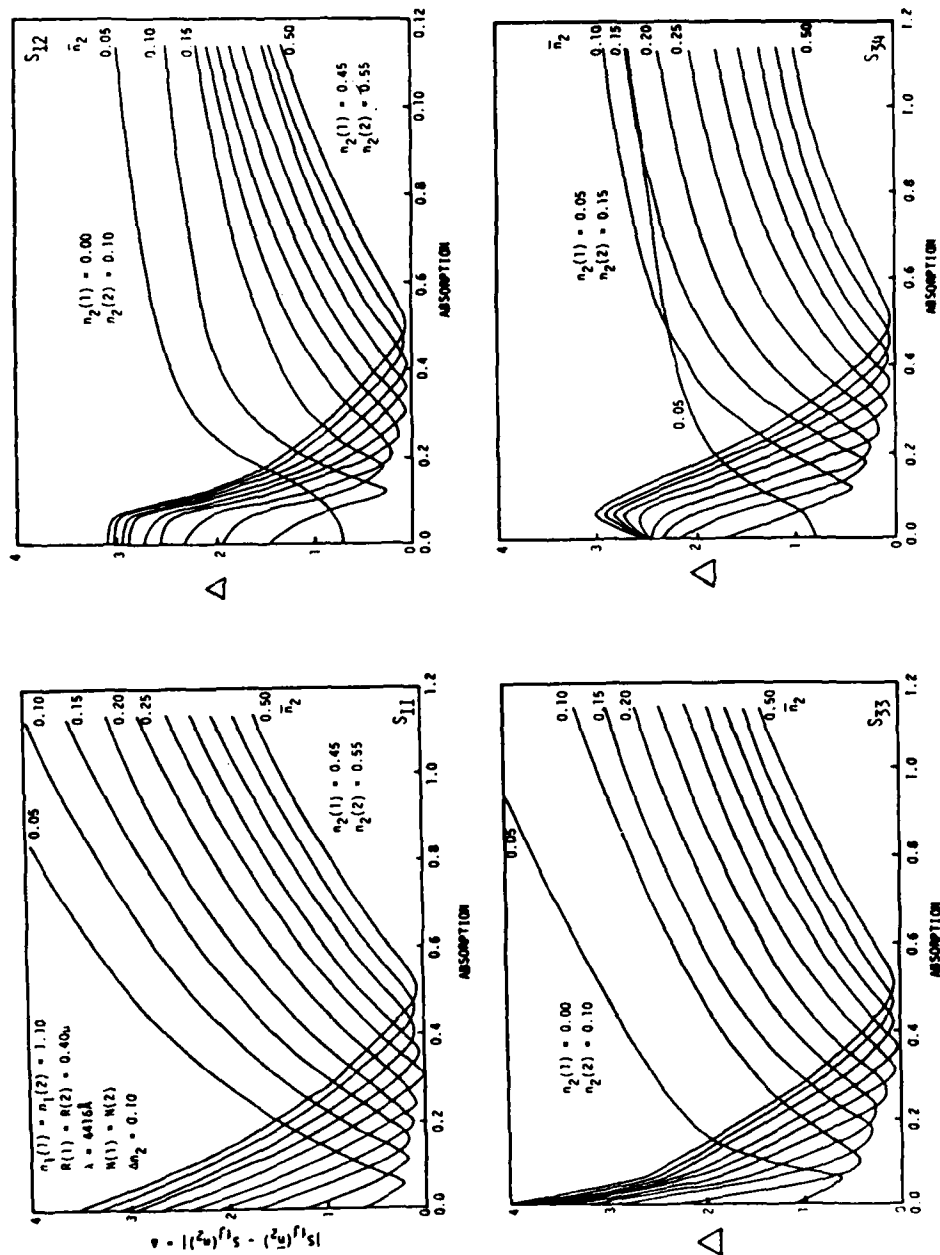


FIGURE 12. Average Absorption of a Two-Component Sphere System

We note that the best fit occurs when $n_2(av)$ of the combination equals n_2 of the single component system. This occurs for all curves and for all S_{ij} . We note also that better fits occur (x is smaller) for higher index particles. In general, all S_{ij} give a decisive "best fit" at the value where $n_2(av) = n_2$, although the fit is not perfect. It is interesting that S_{34} actually increases its x while S_{12} for large $n_2(av)$ remains flat initially as $n_2(av)$ approaches n_2 . We find in general that the average value for absorption is more accurate and meaningful than the average value of refractive index.

In our second experiment we studied the properties of masking of a two-component sphere system. To do this we generate the masking curve shown in Figure 13.

Consider a mixture of two perfect spherical systems:

System (1) = $r(1), n_1(1), n_2(1), N(1)$ (spheres)

System (2) = $r(2), n_1(2), n_2(2), N(2)$ (spheres)

We make mixtures of the above systems in the following ratios:

$$R = \frac{N(1)}{N(2)} = \frac{0}{1} \cdots \frac{1}{512} \frac{1}{256} \frac{1}{128} \cdots \frac{1}{2} \frac{1}{1} \frac{2}{1} \frac{4}{1} \cdots \frac{512}{1} \cdots \frac{1}{0} = \frac{N(1)}{N(2)} = R \quad (5)$$

and then calculate and measure the combination matrix elements $S_{ij}(c)$ for each mixture ratio $N(1)/N(2)$. Note that $N(1)/N(2) = 1/0$ corresponds to the single particle system with matrix elements $S_{ij}(1)$ for (system 1); $N(1)/N(2) = 0/1$ corresponds to the single particle system with element $S_{ij}(2)$ for (system 2). All other $N(1)/N(2)$ represent a mixture of the two pure systems with various ratios represented by matrix elements $S_{ij}(c)$ for the combination. As described above, the combination matrix elements must be properly normalized to account for each component's contribution to the total intensity and polarization. Finally we compute the difference:

$$\Delta = \Sigma |S_{ij}^s(\theta) - S_{ij}^c(\theta)| \quad (6)$$

for all θ for each matrix element and plot Δ as a function of R . The final masking curves obtained are shown in Figure 13. Note that adding particles of system 2 to system 1 generates the masking curve going from left to right, as indicated by the arrows.

Interpretation.

Observe the ratio for which Δ_E crosses each masking curve. Where Δ lies below the experimental detection limit, the region to the left of the vertical dotted line, system 1 particles completely mask system 2 particles. In the region to the right of the dotted line, system 2 particles completely mask system 1 particles. Δ_E represents the experimental limit of resolution ((horizontal) dotted line at Δ_E) and must be established for a particular set of measurements.

The masking curves and the line Δ_E established the range of experimental detection of the two particle systems. For example, a concentration $N(1)$ of a single particle system 1 made up of identical particles with parameters $r(1), n(1), u(1)$ will yield a matrix element signal $S_{ij}(1)$ for

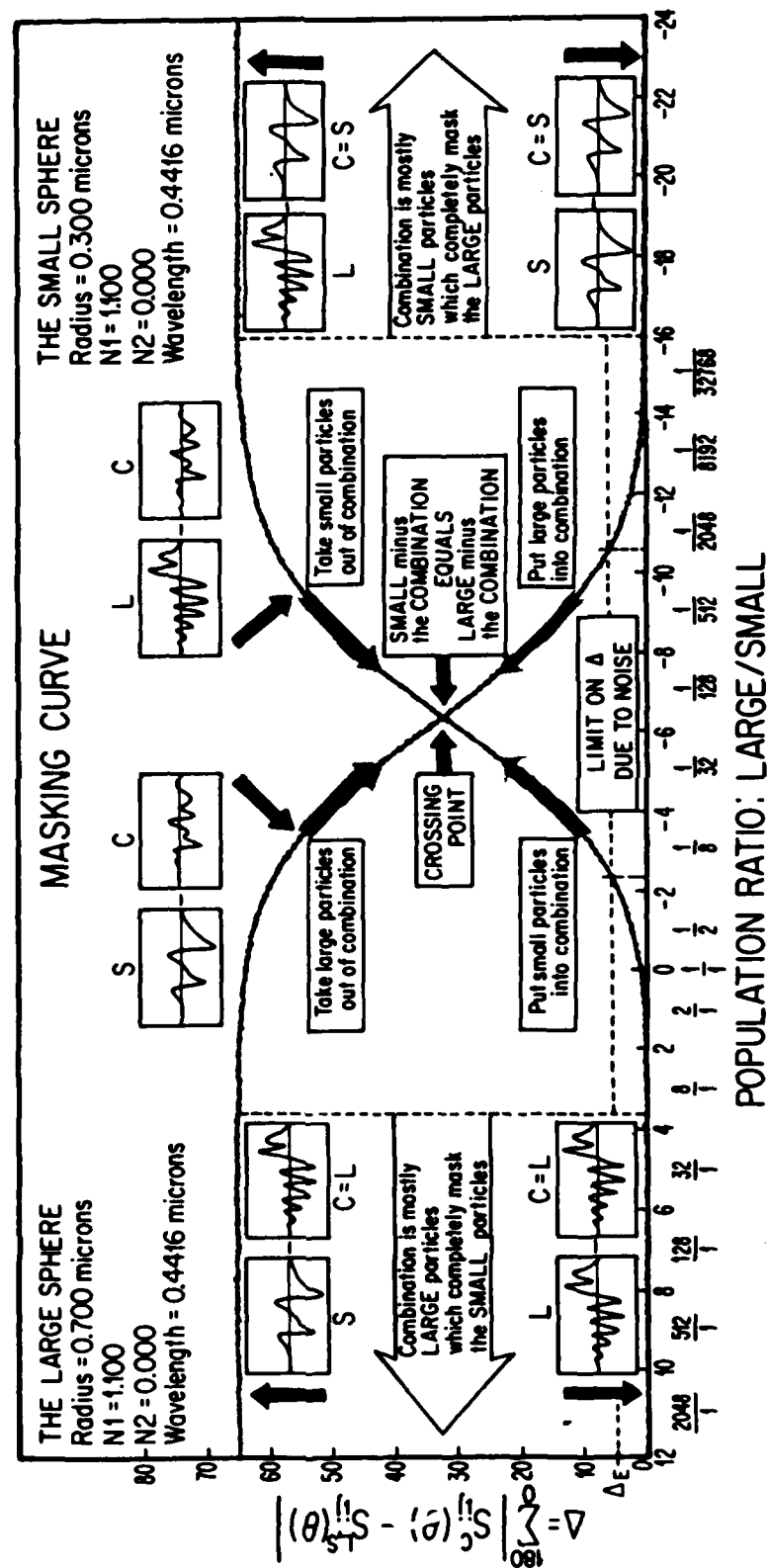


FIGURE 13. Masking Curves for a Two-Component Sphere System

(system 1). This is the starting point, represented by $R = 0/1$ on the left side of Figure 11. This system, when contaminated with $N(2)$ identical particles of system 2 having parameters $r(2)$, $n(2)$, $u(2)$ will yield matrix element signal $S_{ij}(2)$ for (system 2). However, $S_{ij}(c)$ will not be different from $S_{ij}(1)$ until $N(2)$ is large enough to affect the light scattering curves. Therefore, below the threshold ratio $S_{ij}(c) = S_{ij}(1)$ at all angles, and no information about $N(2)$ can be extracted from the combination matrix element signal $S_{ij}(c)$. In this case, particle system 1 completely masks particle system 2 and $S_{ij}(c) = S_{ij}(1)$ for (system 1). System 2 is invisible.

As system 1 is contaminated with particles of system 2, by adding particles of system 2, the $S_{ij}(1)$ for (system 1) will change gradually to the combination matrix element $S_{ij}(c)$ for (system 1 plus system 2) and begin to carry information about system 2 also. Now $\Delta > \Delta_E$. The masking curve, as a function of the ratio $R = N(1)/N(2)$, increases going left to right as R increases.

Further contamination of system 1 by system 2 will gradually make the combination matrix element $S_{ij}(c)$ look like the one for system 2 and finally cause $S_{ij}(c)$ to become exactly $S_{ij}(2)$ for (system 2). When this occurs, particle system 2 completely masks particle system 1 and $S_{ij}(c) = S_{ij}(2)$ for (system 2). Now system 1 is invisible. Regions of complete masking are characterized by the plateaus (zero slope part) of the masking curve, since addition of even more particles will not change the shape of the S_{ij} . Note that if, for a particular matrix element S_{ij} , $\Delta > \Delta_E$ for all ratios, that matrix element will be insensitive to the presence of either particle.

Figure 14 shows the four light scattering curves from a two-component sphere system as a function of relative concentration. The system containing mostly large spheres is characterized by the S_{ij} for 0.7 micron spheres. As more and more small 0.3 micron spheres are added to the system, the original S_{ij} gradually lose phase information and finally become equal to the S_{ij} for 0.3 micron spheres. At certain angles, where both particles have the same polarization, all curves pass through the same point. These crossing points are independent of the population ratio and do not occur at the same angle for all S_{ij} . The single component 0.3 and 0.7 micron S_{ij} curves bound all curves that result from any other population ratio. Data taken at certain (crossing point) angles will show no response to population changes, whereas data obtained at other "well chosen" angles will give large monotonic responses represented by the well known S-shape masking curve. These are the angles that must be selected if the matrix element is to be used as a probe for change.

Figure 15 shows the actual masking curves for the four matrix elements of Figure 14. For this case (and in general), S_{34} is the most sensitive matrix element for monitoring changes in multicomponent systems. S_{34} shows the largest absolute difference when masking is complete, and it has the largest slope (difference change with respect to system change), in this case near the ratio $1/64$. Numerical data show that S_{34} is more than twice as sensitive as the other S_{ij} at threshold, in this case where $N(2)/N(1) = 4/1$. For an instrumental detection level (or noise) set at 0.05, system changes can be detected only between population ratios $1/8$ to $1/1024$, a factor of 128.

LIGHT SCATTERING FROM A TWO COMPONENT SPHERE SYSTEM

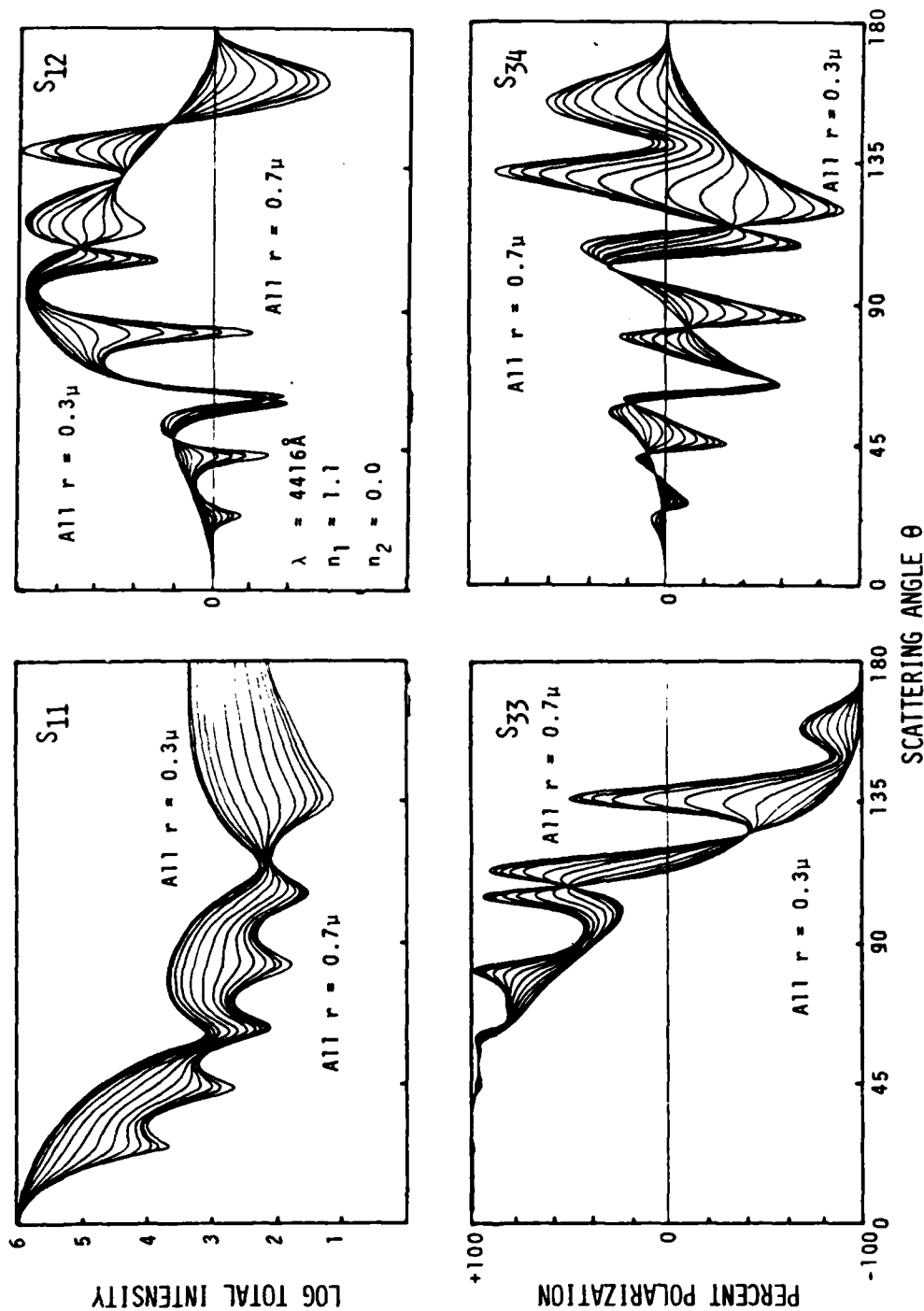


FIGURE 14. The Four Matrix Elements from a Two-Component Sphere System as a Function of Relative Population

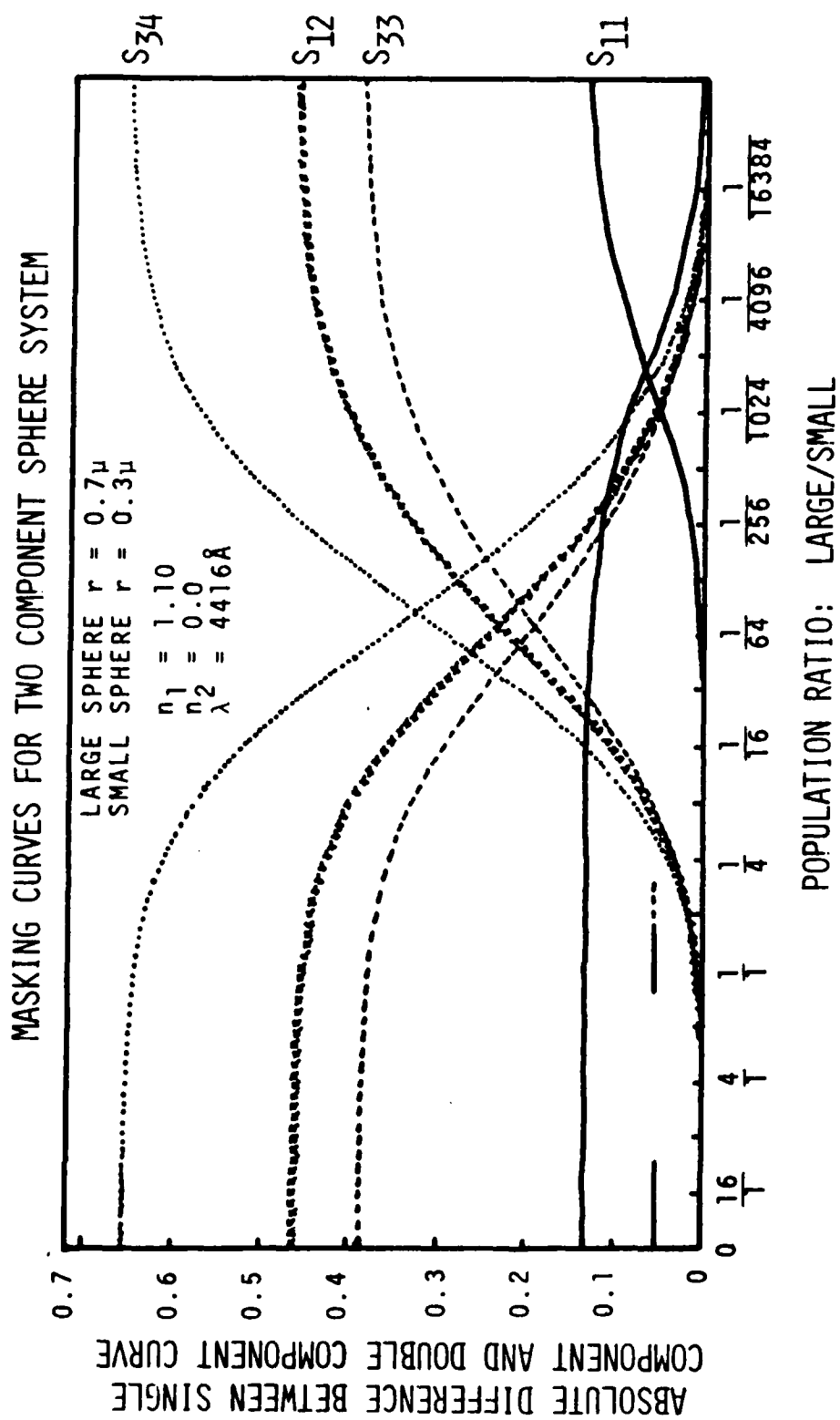


FIGURE 15. The Four Masking Curves for a Two-Component Sphere System

2.4 Quartz Calibration Fibers.

We have standardized our techniques for producing high quality, quartz fibers for the calibration of nephelometers and other light scattering instruments. The fibers are characterized by the following parameters:

real refractive index	$n_1 = 1.466$
imaginary index	$n_2 = 0.000$
radius	$r = 0.2$ to > 5 microns
length	$l = 1 - 5$ cm

The fibers have a circular cross section whose radius is determined by a best fit to theoretical curves. This technique gives the radius to better than 0.1% (1 nanometer in 1 micron fiber), making them useful as calibrators.

Fibers are single "perfect" particles. They can be permanently mounted on a frame, stored in a safe place and used over and over again. They can be geometrically manipulated (tilted, bent, and rotated) reversibly, and are devoid of the problems of polydispersivity, clumping and irregularity that characterizes systems or collections of perfect spheres.

Figure 16 shows the 4 experimentally measured matrix elements of a perfect fiber and the best fit to theoretical curve. The fiber radius is 1.02 microns. Figure 17 shows a mounted fiber fastened to the lid of a container which can survive transit through the US Mail!

2.5 Scattering from Geometrically Perturbed Quartz Fibers.

The simplest but yet significant perturbation that can be given to a perfect fiber is an exactly known geometrical distortion. Geometrical distortions such as tilting, bending, and rotation can be carefully controlled and exactly characterized. They are reproducible, reversible, and amenable to exact theoretical treatment.

Fiber diffraction patterns are extremely sensitive indicators of fiber parameters. Two similar micron size fibers could look identical when viewed through a microscope, yet give diffraction patterns that are very different. Extremely small variations in the fiber size, cross-sectional shape, optical constants, and illumination geometry which cause indiscernible changes in their image can cause significant changes in their diffraction patterns. To understand fiber scattering characteristics in a completely controlled laboratory situation, we manipulated a fiber's geometric illumination, morphology, and geometry while examining diffraction patterns and relating them to fiber parameters.

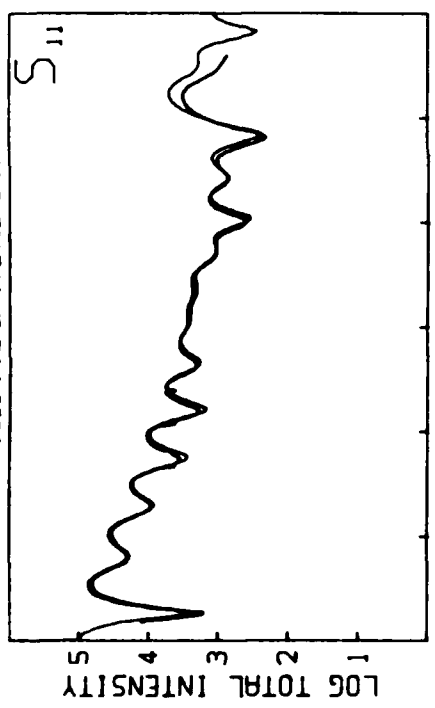
We did four experiments to examine the response of a fiber diffraction pattern while a perfect fiber was subjected to geometrical perturbations. To produce the perturbations, the fiber was rotated, bent, bent and rotated, and tilted in a laser beam.

Figure 18a shows the experimental apparatus used to identify and select a so-called perfect fiber for further study. The 40-micron diameter quartz fiber is illuminated by a HeNe laser beam ($\lambda 6328\text{\AA}$) while it is rotated about the Z axis at one rotation per 3 minutes by motor. The light scattering pattern is recorded on photographic paper located on a screen 450 mm downbeam from the fiber on the X-Z plane. The photographic paper simultaneously moves in the Z direction 1 inch per 45 seconds. An almost perfect fiber with uniform cross-section, produces a diffraction pattern which remains almost constant

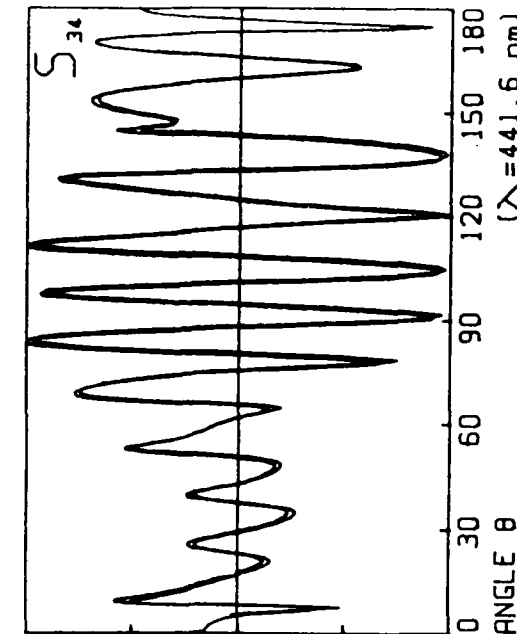
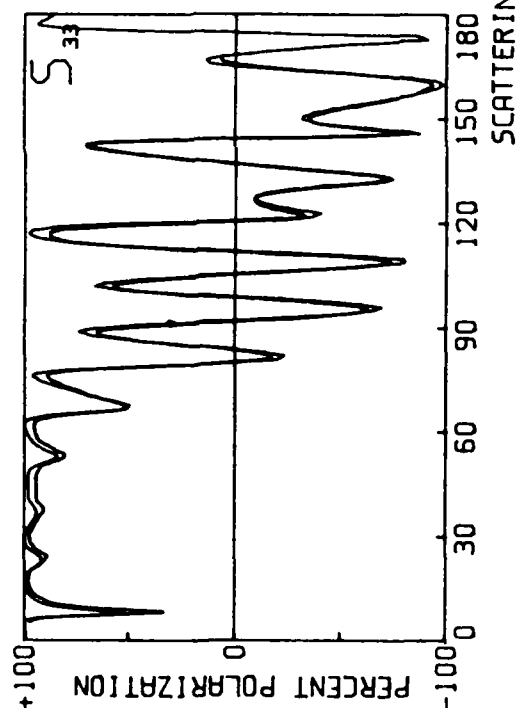
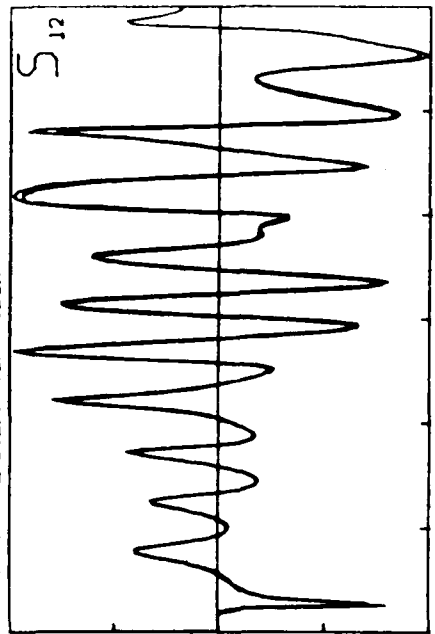
CALIBRATION FIBER

8/14/1984
GVV

— THEORY FOR .999 MICRON RADIUS QUARTZ FIBER



— QUARTZ CALIBRATION FIBER



($\lambda = 441.6 \text{ nm}$)

FIGURE 16. Experimental and Theoretical Fits of the Four Matrix Elements from a Calibration Fiber



FIGURE 17. Photograph of Mounted Fiber and
Its Container

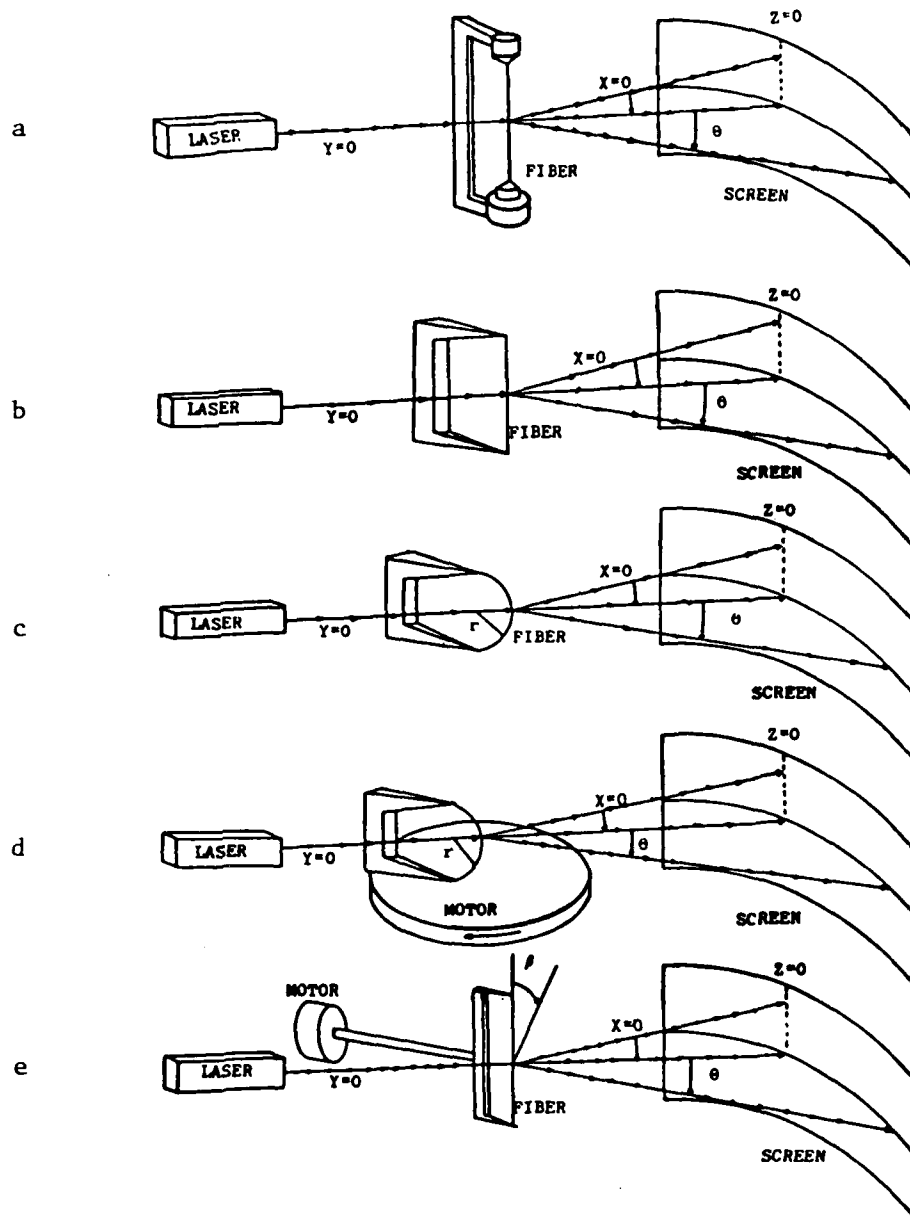


FIGURE 18. Experimental Setup to Study Bent, Rotated and Tilted Fibers

during one rotation, as shown in Figure 19. A perfect fiber, which scatters light that is exactly predicted by theory, is the logical starting point for fiber scattering studies. We used one for further experimentation, as described in the next sections.

2.5.1 Scattering From a Bent Fiber.

Figure 18b shows the experimental apparatus used to study the diffraction pattern as a function of fiber bend. The fiber, illuminated as described by Figure 18a, is connected across two supports which, when brought together, bend the fiber into a predetermined radius, r . As the fiber is bent, its diffraction pattern is recorded on photographic paper in a series of photographs, one for each particular fiber bend radius. The results are shown in Figure 20.

2.5.2 Scattering as a Function of Bend and Rotation.

Figure 18c shows the experimental apparatus used to study the diffraction pattern of the fiber bent with radius $r = 7.94$ mm as a function of the fiber rotation angle. The fiber holder can turn the fiber about the Z axis. As the fiber is rotated through angle θ , a specific scattering pattern is recorded in a series of photographs each at a specific rotation angle. The results are shown in Figure 21.

2.5.3 Scattering as a Function of Tilt.

Figure 18d shows the experimental apparatus used to study the diffraction pattern of the fiber as a function of tilt in the Y-Z plane. The fiber is attached perpendicularly to a holder which rotates about the X axis, which is also perpendicular to the laser beam. As the fiber is tilted through angle β , its scattering pattern is recorded in a series of photographs each taken at specific tilt angle β . The results are shown in Figure 22.

2.5.4 Results and Discussion.

The effects of bending are seen in Figure 20. First, we note that the max/min locations along the X axis of the diffraction patterns are independent of fiber bend. This information, therefore, can be used to measure the fiber diameter, giving the same value as that from an unbent fiber.

Second, bending the fiber causes additional interference along the Z axis and out of the scattering plane. Perfect fibers scatter light perpendicular to the fiber axis, whereas deformed fibers scatter out of the plane. In this case the exactly known deformity is the bend.

Third, a "focus" is formed in the diffraction pattern on the concave side of the fiber. The distance, D , from the center of the diffraction pattern ($\theta = 0$) to the focus ($\theta > 0$) is proportional to the radius r of the fiber bend, ($D = kr$).

The effects of rotating bent fiber are seen in Figure 21. First we note that the max/min locations vary with fiber rotation. The minima locations on the concave side of the fiber move towards the center ($\theta = 0$) while the minima locations on the convex side move away from the center as angle θ approaches 90° .

2.7 Response of Matrix Elements to Changes in Absorption and Refractive Index.

Figures 30a-30b summarize a study of the response of light scattering curves to refractive index, absorption, and spherical particle size. These curves are for single component monodispersed sphere systems.

Figures 30a-30c show the total intensity (matrix element S_{11} , scattered from perfect spheres with $n_1 = 1.10$ for three different absorptions $n_2 = 0.00, 0.04$, and 0.40 as a function of sphere radius (0.10 to 1.0 microns). We observe the following:

Figure 30a. For relatively low index particles ($n_1 = 1.1$) the total scattered intensity (area under the curve) increases by over 5 orders of magnitude as the particle size increases from $r = 0.10$ to 1.0 microns. The intensity in the forward scatter ($\theta < 180^\circ$) increases monotonically over 8 orders of magnitude, making it a good indicator of particle size and size change. The forward scatter to backscatter intensity ratio, which is 1 for small particles, increases to over 4 orders of magnitude for larger particles. This ratio is the main, and sometimes the only, indicator that irregular scatterers are large compared to the wavelength of light. The backscatter intensity at 180° , and for all angles larger than 180° , does not react monotonically with particle size, making the backscatter a poor probe of particle size and change. Data like these show, for example, that 0.10 micron spheres in the ratio of 10^8 to 1 will mask the large sphere information in the backscatter ($>90^\circ$). Large spheres can be hidden effectively by many small spheres. Also, small spheres can be hidden effectively by very few large spheres. This effect puts a high demand on the purity of small scatterers whose light scattering signals can be masked or destroyed by the contamination of just a few large particles.

Figure 30b. Increasing absorption slightly from $n_2 = 0.0$ to 0.04 has little effect on the scattering except to decrease slightly the backscatter intensity which still is not monotonic to size change.

Figure 30c. Increasing absorption significantly by an order of magnitude from $n_2 = 0.04$ to 0.40 causes significant changes. The oscillatory structure almost disappears in the backscatter which now varies almost monotonically with particle size, as does the forward scatter. Even light scattered from the small Rayleigh particles ($r = 0.10$ micron) has increased by over 1 order of magnitude.

In general, increasing the absorption of relatively low index particles increases the amount of backscatter and washes out the valuable oscillatory phase information which is often used to determine particle size.

Figures 30d-30f show similar total intensity curves for the same three different absorptions $n_2 = 0.0, 0.04$, and 0.40 , but for spheres of large refractive index $n_1 = 1.70$, we observe the following:

Figure 30d. For relatively high index particles ($n_1 = 1.7$) the intensity in the forward scatter ($\theta < 180^\circ$) increases by more than 6 orders of magnitude but not monotonically as with low index spheres. Also, there is significantly increased backscatter with increasing particle size approaching a ratio (forward:back) of less than 10. In fact, slightly polydispersed large Mie particles give curves that are similar to the small Rayleigh ($n_1 = 1.1$) spheres.

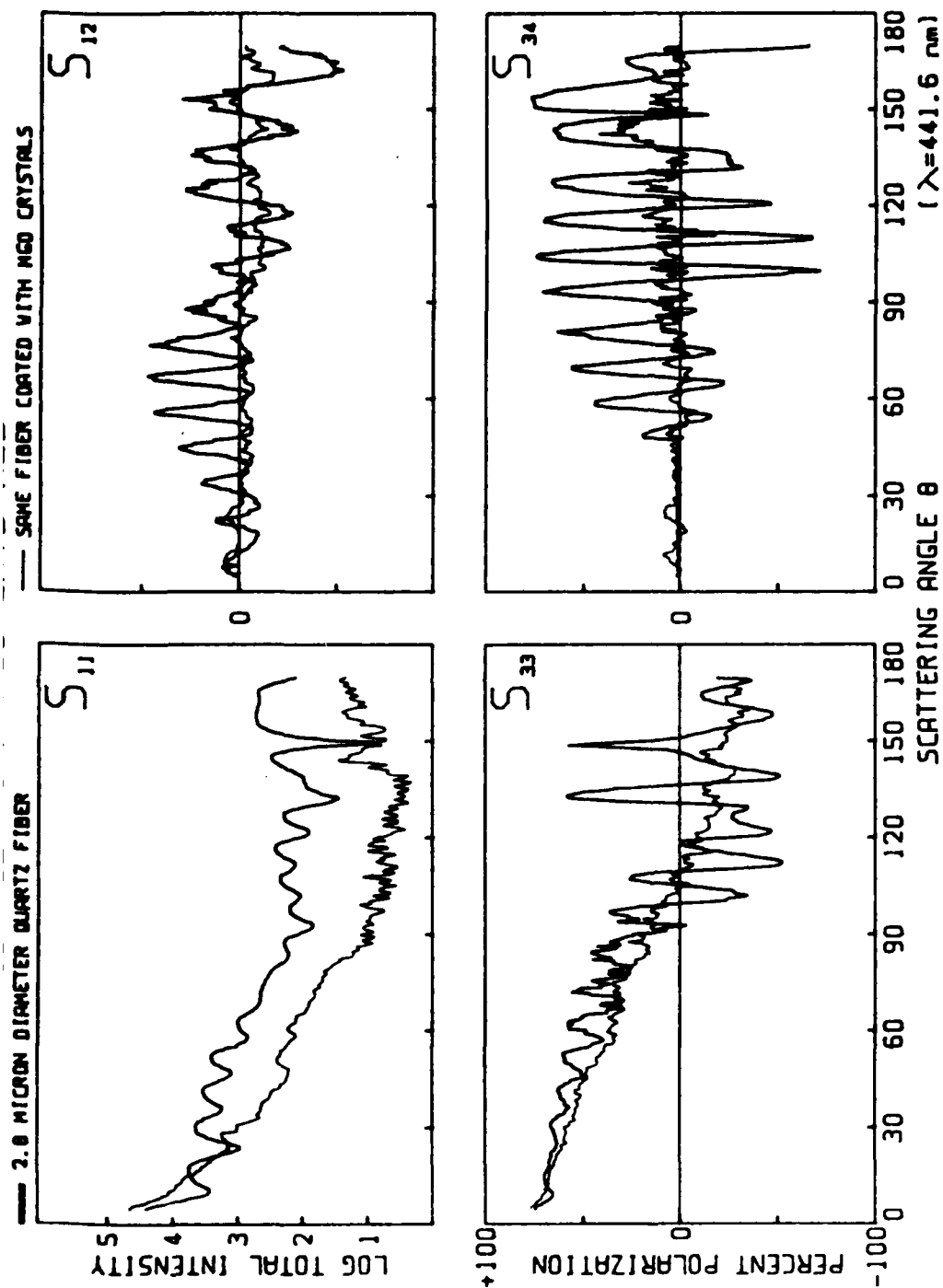


FIGURE 29. Matrix Elements from an Uncoated and MgO coated Quartz Fiber

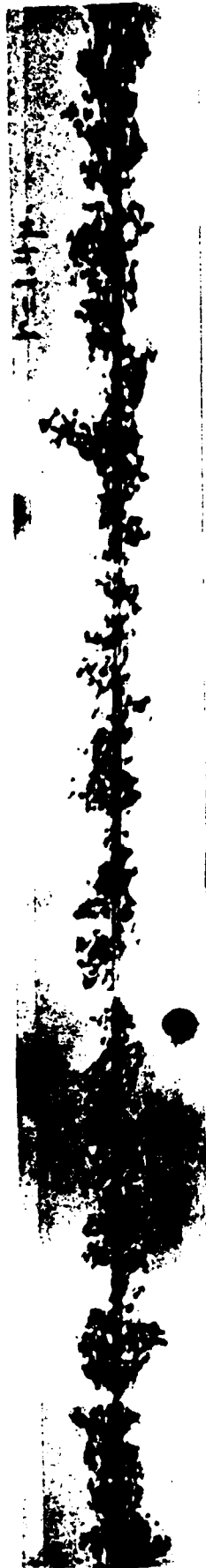


FIGURE 28. Photomicrograph of a 2.8 Micron Diameter Quartz Fiber Coated with MgO Crystals

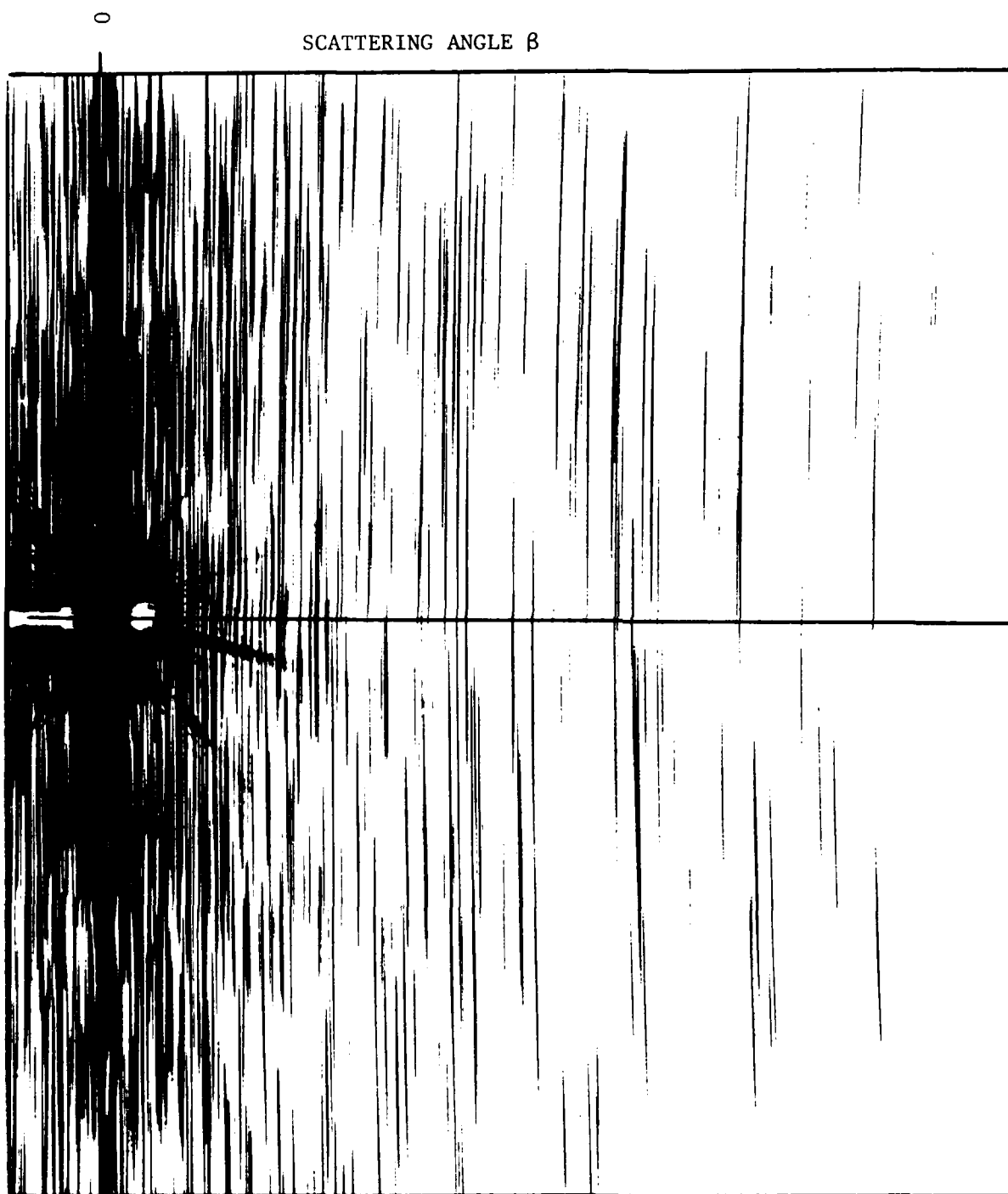


FIGURE 27. Light Scattering out of The Scattering Plane by a Rough Quartz Fiber

LIGHT SCATTERING FROM A ROUGH SURFACE QUARTZ FIBER

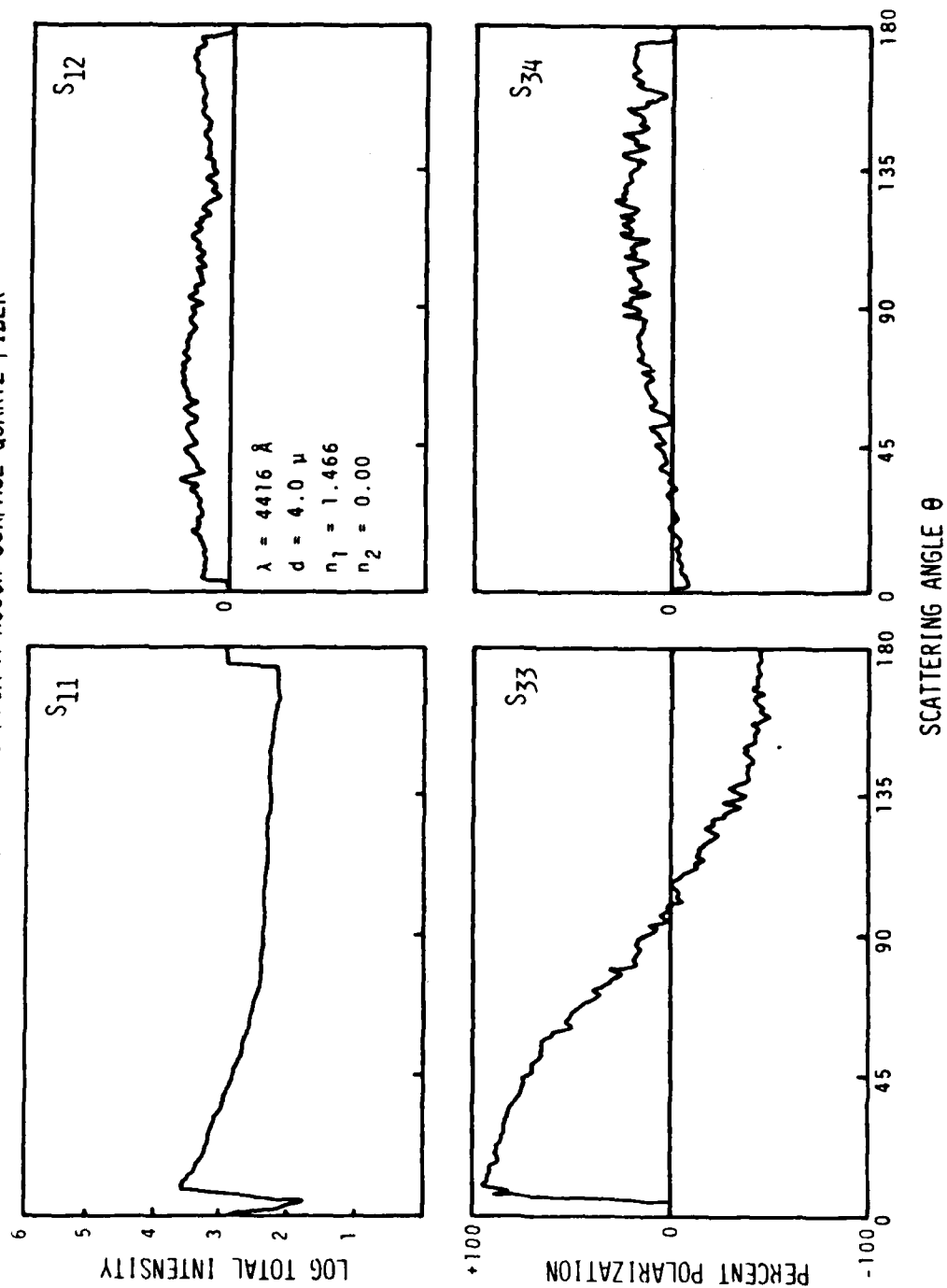


FIGURE 26. Matrix Elements of Rough Quartz Fiber of Figure 25

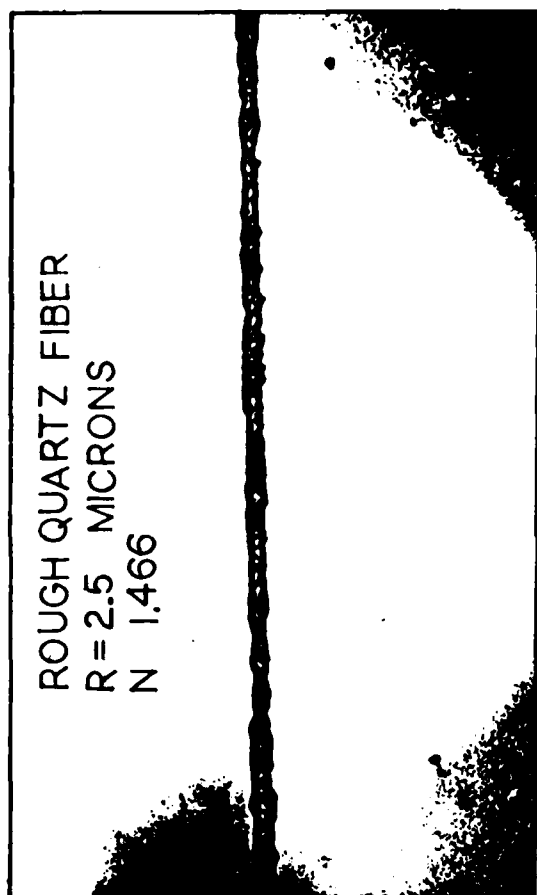


FIGURE 25. Photomicrograph of a Rough Surface Quartz Fiber

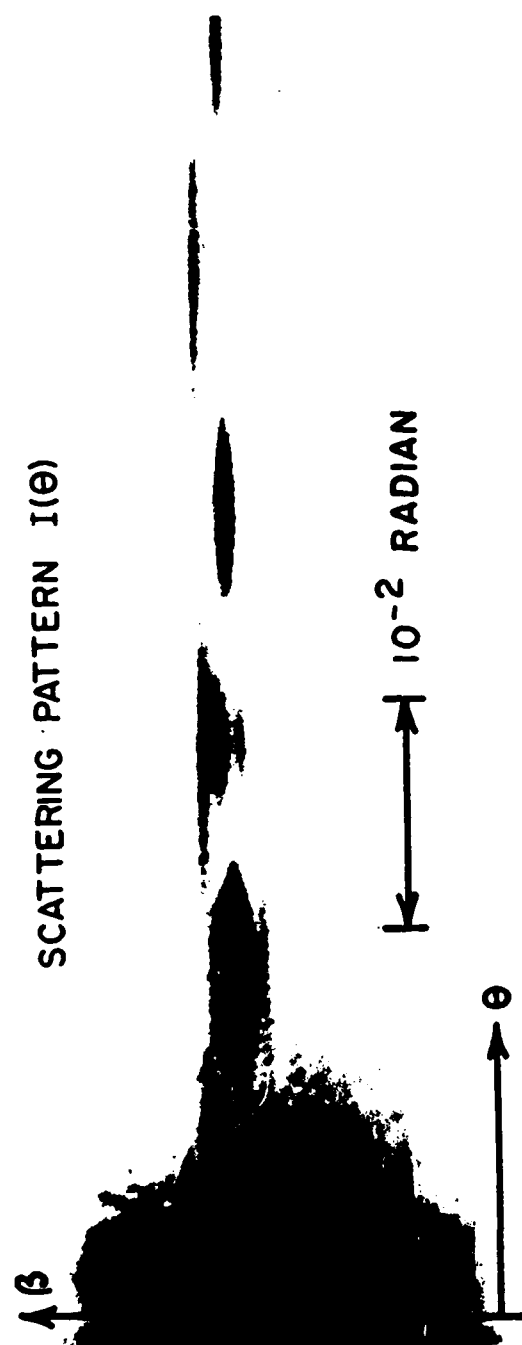


FIGURE 24. Light Scattering Pattern (S_{11}) From an Apparently Perfect Fiber

rough surface particles--(Arizona road dust). It is instructive to visually examine the scattering patterns created by apparently perfect fibers. Figure 24 is a photograph of the total intensity diffraction pattern from a "perfect" fiber. The nature of the imperfection could not be detected or determined by examination with a light microscope. The photograph shows how phase information can become confused when light is scattered from a slightly imperfect fiber. Scattering occurs both in the θ direction, perpendicular to the fiber, and in the β direction, out of the scattering plane. A detector scanned in the θ direction would average over the intensity scattered in the β direction, and thereby create a loss of θ -phase information. Experimentally measured matrix element curves from imperfect quartz fibers of known radius and optical constants do not fit the theoretical curves for perfect fibers. The phase information is almost totally destroyed, and that which remains does not necessarily coincide with that from the perfect fiber. More severe perturbations create even more severe phase loss.

We have studied the loss of phase information in the S_{ij} from two quartz fibers that have had their surfaces artificially roughened.

One is an $r = 2.5$ micron quartz fiber that had its surface roughened during its manufacture. A photomicrograph is shown in Figure 25. All four nonzero matrix elements, shown in Figure 26, are smooth and devoid of the phase information to determine fiber size. S_{12} and S_{34} are almost zero. The light scattering pattern shown in Figure 27 is characterized by extreme, out of the θ -plane scattering.

The other is a perfect 1.4 micron quartz fiber that we coated with small (<0.2 micron) MgO crystals. A photomicrograph is shown in Figure 28. The four nonzero matrix elements are shown in Figure 29.

Matrix element S_{11} shows that the total scattering in the θ plane decreases. This is due to increased out-of-plane scattering and some absorption by the MgO crystals. The remaining phase information is barely sufficient for determining the fiber size. The "high frequency" oscillations are noise, due more to the random scattering by individual MgO particles than by the increased diameter due to coating.

Matrix elements S_{12} and S_{33} are almost smooth. Increased roughness drives S_{12} toward zero, and not toward the usual sin squared curve for Rayleigh particles. S_{33} is slightly flatter than the S_{33} for Rayleigh particles. Both curves show a hint of phase information from which the diameter of the uncoated fiber can be determined. Matrix element S_{34} is almost zero everywhere, but like S_{12} and S_{33} , it contains some phase information.

It is obvious and significant that while increasing roughness destroys phase information, it does not create Rayleigh shaped signals for the S_{ij} in the limit of extreme polydispersivity or surface roughness. This same behavior is observed for polydispersed sphere and irregular particle systems. It is important to point out that the matrix element bounds at 0° , 90° , and 180° that hold for spheres do not hold for fibers. S_{12} and S_{34} are not necessarily zero, and S_{33} is not necessarily $\pm 100\%$ at 0° and 180° as they are for spheres, regardless of size.

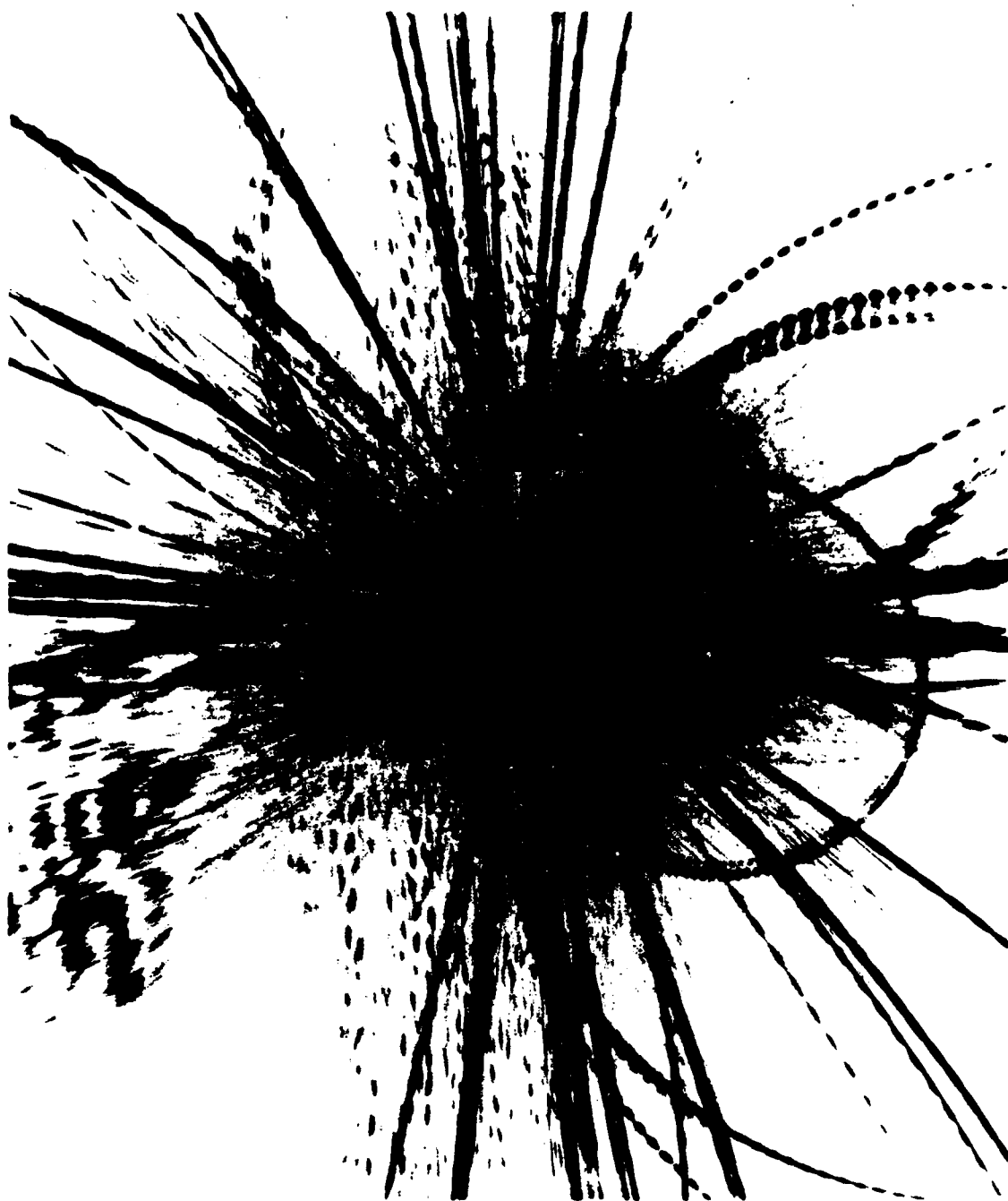


FIGURE 23. Light Scattering Pattern (S_{11}) from a Complex Collection of Random Fibers

Second, as angle θ approaches 0° , intensity changes occur in each diffraction pattern. However they are not as significant as the increase asymmetry about the X axis. A twisting, or overlapping occurs in the diffraction pattern itself. This irregularity makes it difficult to determine the thickness of bent fiber because the max/min locations are not well defined along the scattering pattern.

The effects of fiber tilting are seen in Figure 22. First, tilting the fiber through angle β creates a diffraction pattern described by various conic sections. At $\beta = 0$, a straight line in the X-Y plane is formed. When $0^\circ < \beta < 45^\circ$, a hyperbola is formed; when $\beta = 45^\circ$, a parabola is formed; when $\beta > 45^\circ$, an ellipse is formed; and when $\beta = 90^\circ$ (the limiting case), a circle is formed. For this case the laser beam would hit the fiber head on, leaving only a single point for the diffraction pattern.

Second, the diffraction pattern of a perfect fiber should remain symmetric as the fiber is tilted. The pattern becomes asymmetric at $\beta = 84^\circ$ simply because this perfect fiber is not completely perfect. In spite of the small asymmetries, the overall pattern changes significantly as β changes. Individual interference beats (max/min) occur as before on the curved X axis. The asymmetries formed by the tilting of a perfect fiber are very sensitive indicators of fiber perfection.

2.5.5 Conclusion.

Light scattered from perfect fibers forms diffraction patterns that are much more complex than first suspected. Pure geometrical manipulations of the fiber are very basic and easily controlled perturbations, which affect both the total intensity and the geometrical distribution of the scattered light. The effect of these exactly known perturbations of perfect fibers can be used to learn about non-perfect fibers.

These total intensity light scattering patterns (matrix element S_{11}) point out the difficulty of measuring the scattered light with a polar nephelometer. The detector would have to move in the proper path described by the conic section as well as aim toward the fiber. The slit (or circular aperture) will still be collecting light from various overlapping sections of the diffraction pattern.

Perfect fibers and well-characterized perturbations should be studied to increase our fundamental knowledge of small particle scattering. In biology, scattering from muscle fibers and nerve tissue while undergoing biological activity can give information about their structure. Some biological changes can be detected only by light scattering techniques.

Our concluding Figure 23 shows a very complex scattering pattern from a complex system of fibers. The previous experiments explain how various individual fibers in the system create the diffraction pattern. It is obvious that this pattern is an image created by a collection of many bent and tilted fibers.

2.6 Rough Fiber Scattering.

Phase information on matrix element signals is lost as the individual particles or scattering systems become more irregular. This has been shown for polydispersed spheres--(an irregular system of perfect particles) and

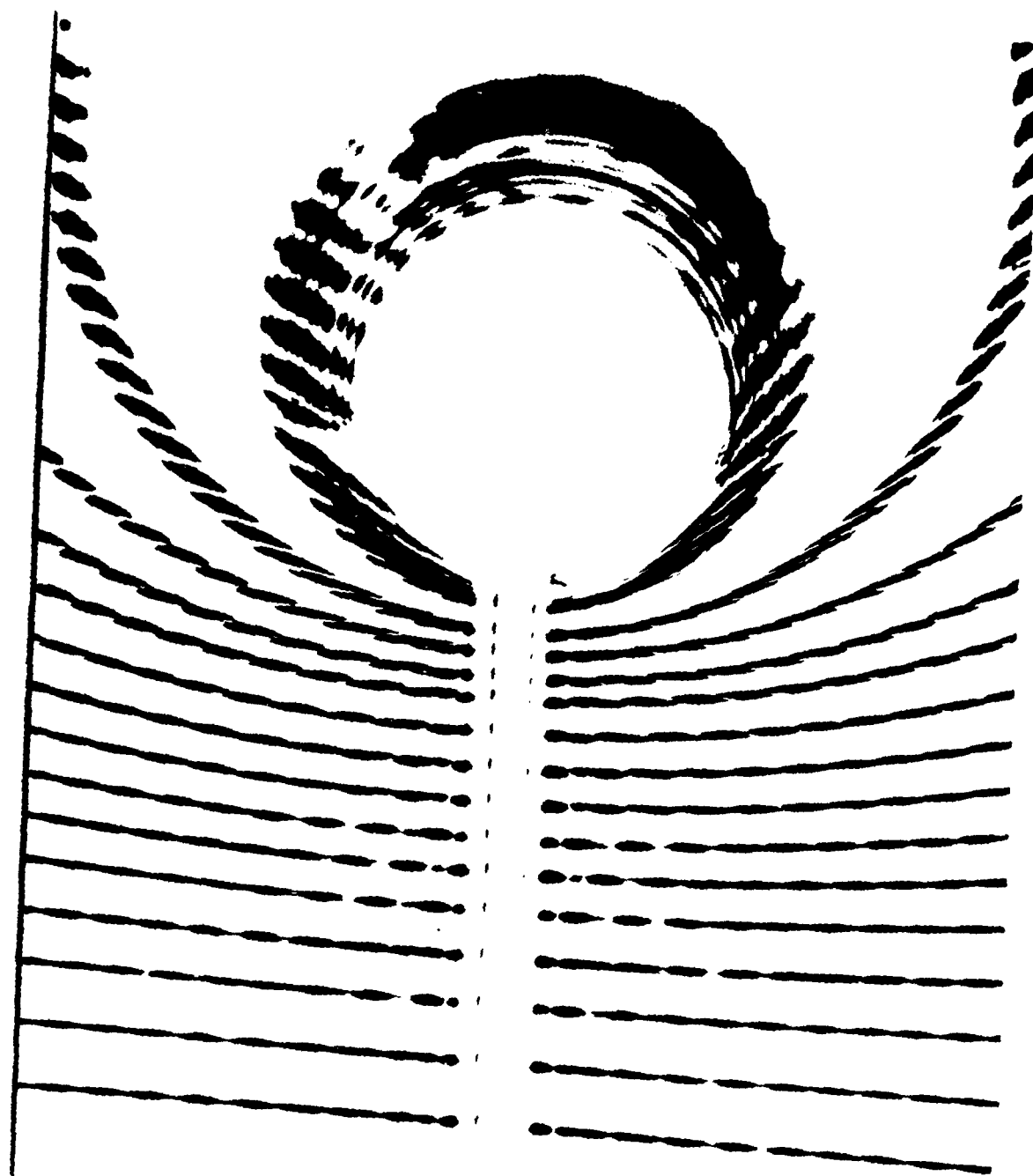


FIGURE 22. Light Scattering Patterns (S_{11}) as a Function of Fiber Tilt

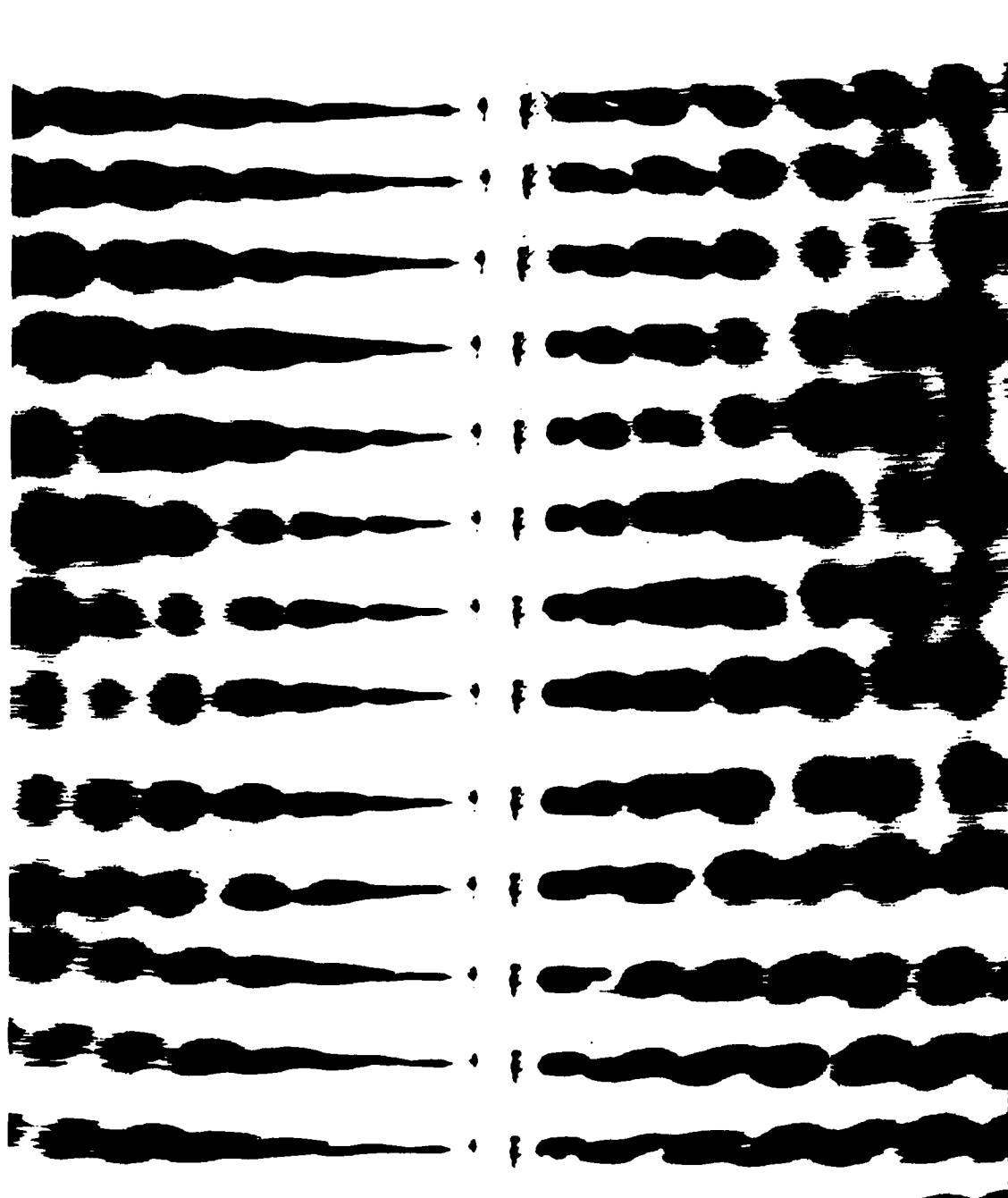


FIGURE 21. Light Scattering Pattern (S_{11}) as a Function of Bent Fiber Rotation

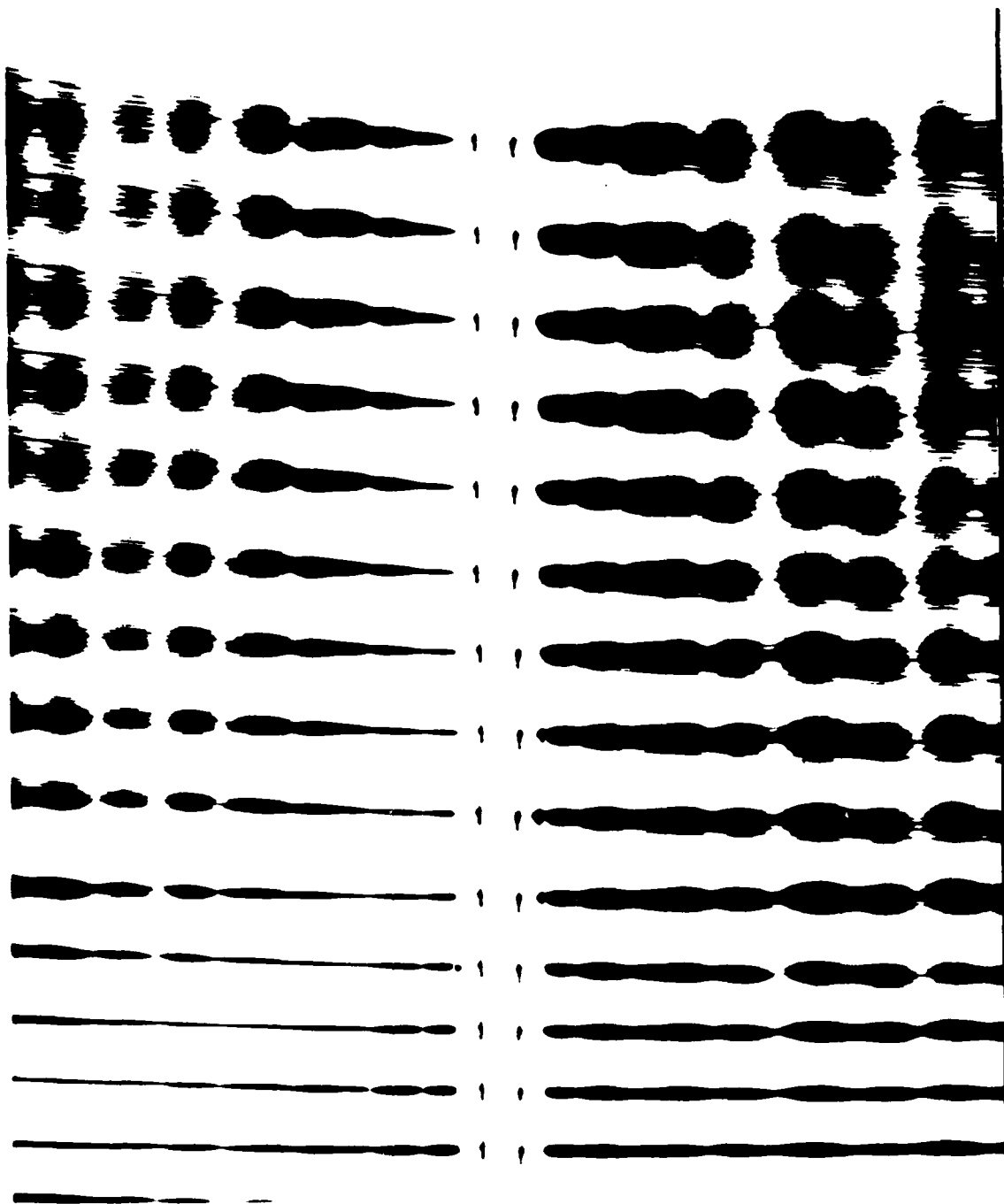


FIGURE 20. Light Scattering Patterns (S_{11}) as a Function of Fiber Bend

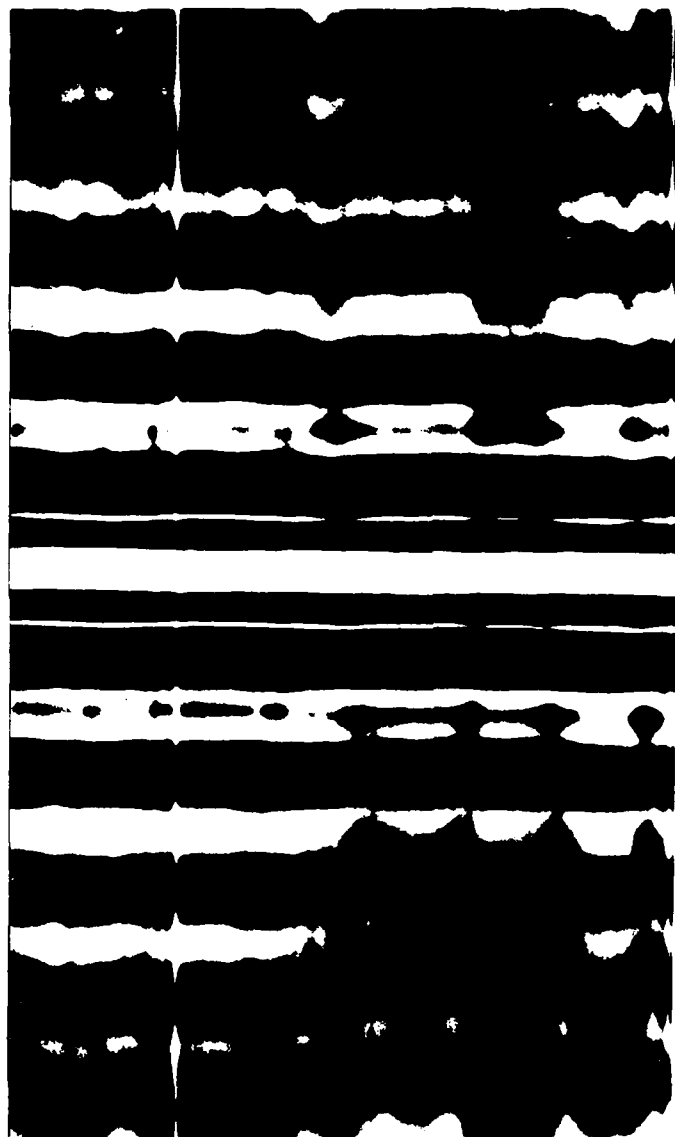


FIGURE 19. The Variation of Light Scattered from a "Perfect" Fiber as a Function of Rotation Angle θ

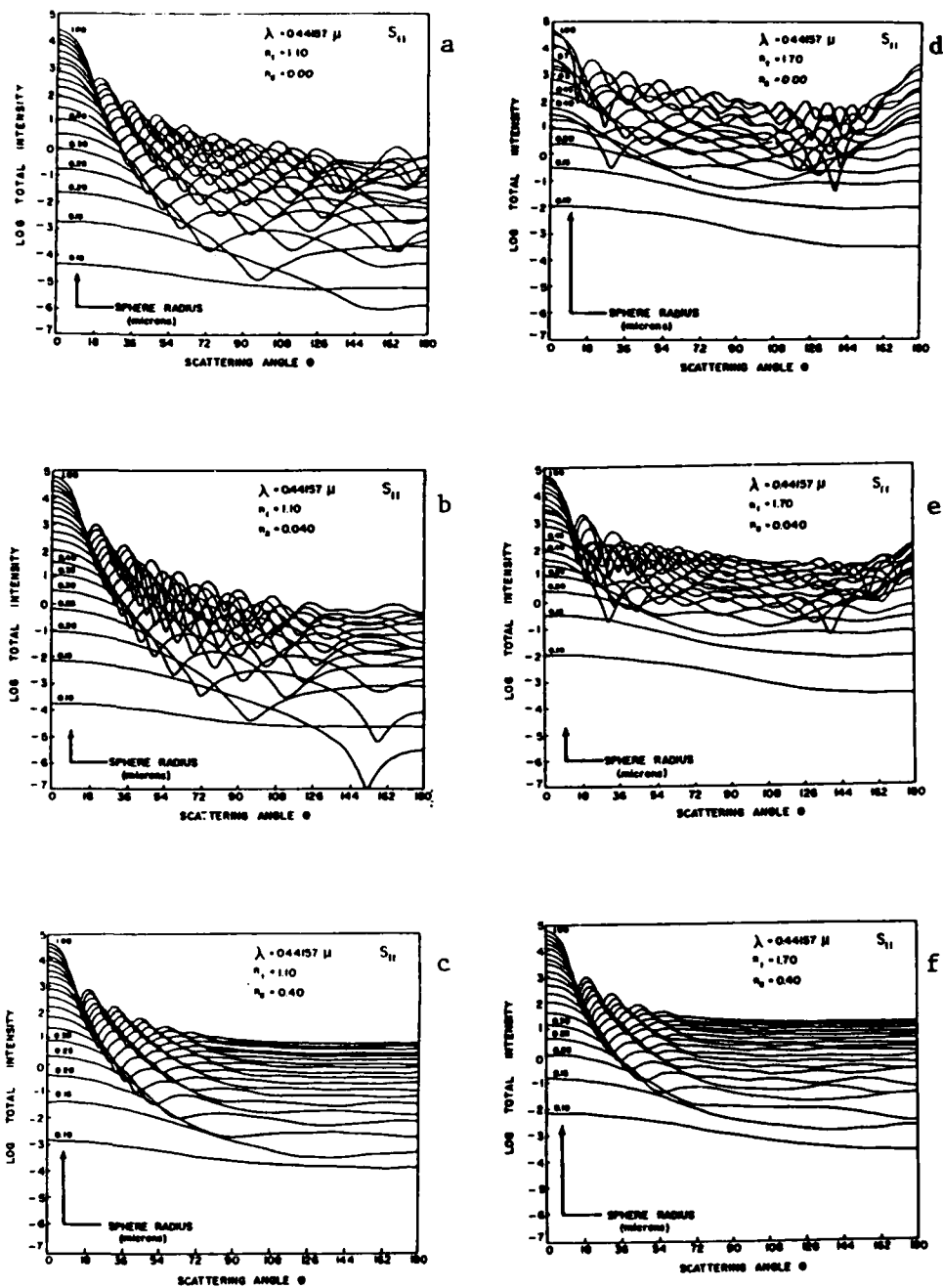


FIGURE 30. S_{11} Matrix Elements as a Function of Size, Refractive Index and Absorption

Figure 30e. Increasing absorption slightly from $n_2 = 0.0$ to 0.04 has little effect except to lower the total intensity scattered by the larger particles.

Figure 30f. Increasing absorption significantly from $n_2 = 0.04$ to 0.40 destroys virtually all oscillatory phase information in the backscatter as it did for the low index particles. In fact, the curves of Figure 30f are almost identical to those of Figure 30c, showing that when absorption is high it dominates the light scattering curves. Therefore, high absorption effectively masks out all information about the particle's refractive index regardless of its magnitude. This also means that a small change in refractive index would go undetected in the total intensity signal.

To examine further the role of the refractive index, we generated Figures 31a-31c which show the total intensity scattered from 1.0 micron spheres as a function of refractive index n_1 for three different absorptions $n_2 = 0.0, 0.05, \text{ and } 0.50$.

Figure 31a. ($n_2 = 0.0$) As n_1 increases, the relative amount of light in the backscatter increases over 4 orders of magnitude. Large spheres, polydisperse in R and n_1 , would interfere to give relatively smooth curves containing little phase information similar to small particle Rayleigh curves.

Figure 31b. ($n_2 = 0.05$) Increasing absorption slightly washes out the backscatter phase information for angles greater than 90° . Note the curve for $n_1 = 1.00$ is that for an "index matched" particle which scatters only because of its absorption. Increasing n_1 destroys even more phase information toward the forward scatter and increases the amount of backscatter by over 2 orders of magnitude.

Figure 31c. ($n_2 = 0.50$) Large absorption, large index particles give curves which are essentially Airy functions--diffraction patterns from circular apertures. In the forward scatter the curves are essentially independent of n_1 . The only response to change in n_1 occurs in the backscatter.

2.7.1 Matrix Elements As Probes of Small Perturbations .

We investigated the use of matrix elements as a probe for change in particle property. An ideal probe would respond linearly to a linear change in a particle property. For real probes, any response will at first be linear (by definition), then non-linear but single valued, and finally oscillatory (multivalued), or flat (showing no response at all). A summary of the expected response is displayed in Figure 32, where "any feature" of an S_{ij} curve is plotted as a function of the strength of perturbation.

2.7.2 Size, Refractive Index, Absorption, and Wavelength .

Figures 33 and 34 show the actual responses of the matrix elements resulting from "perturbation" of some optical and geometrical properties.

Figures 33a and b show the S_{ij} response at $\theta = 90^\circ$ as the radius of sphere changes from 0.4 to 0.6 microns (at constant wavelength) and as the illuminating wavelength changes from 0.4 to 0.6 microns (at constant radius). All S_{ij} display the features shown in Figure 32. With the exception of a small wavelength-dependent index n_1 , Figures 33a and b can be matched quite well if the radius scale is plotted in the opposite direction. This occurs because

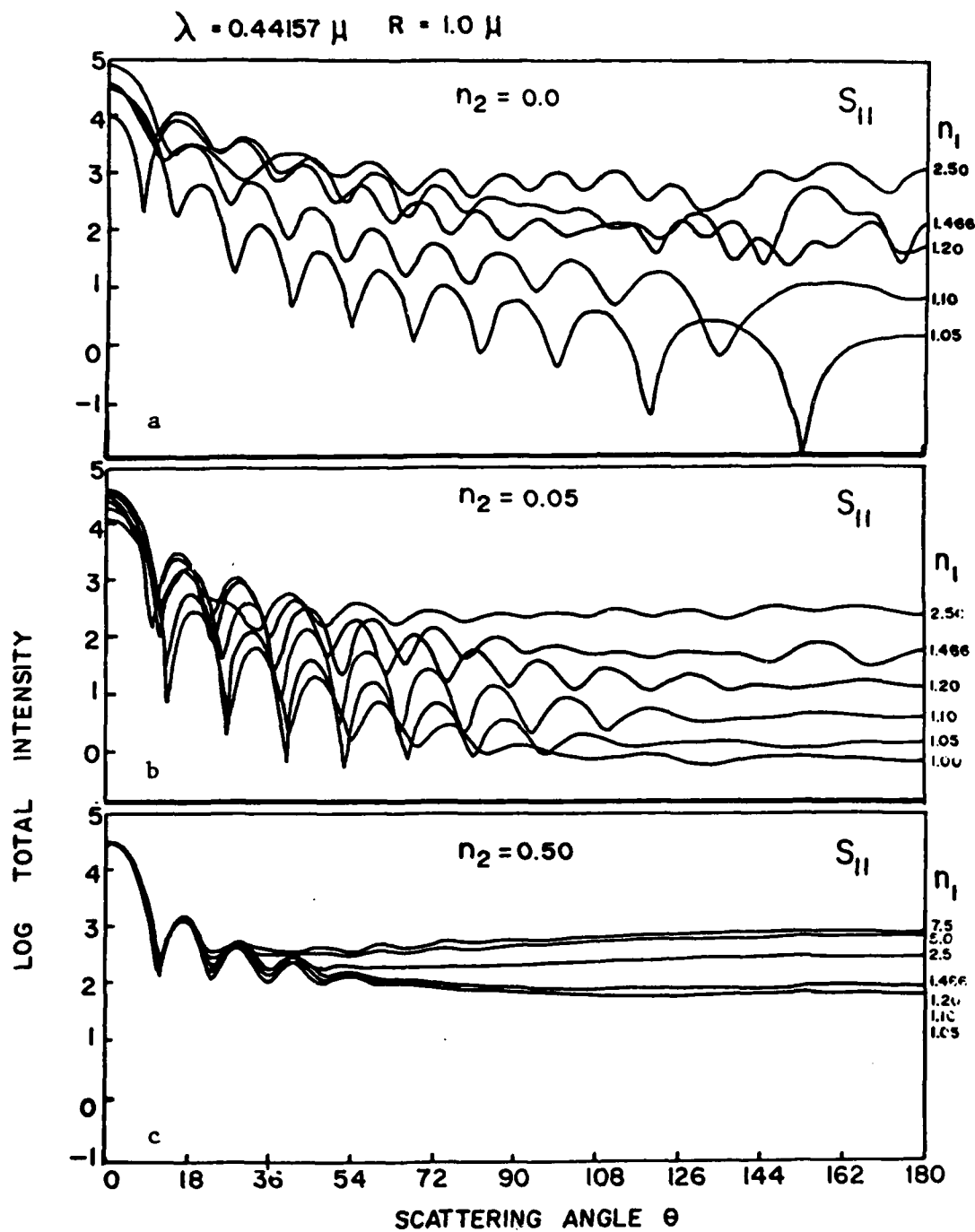


FIGURE 31. S_{11} Matrix Elements as a Function of Absorption and Refractive Index

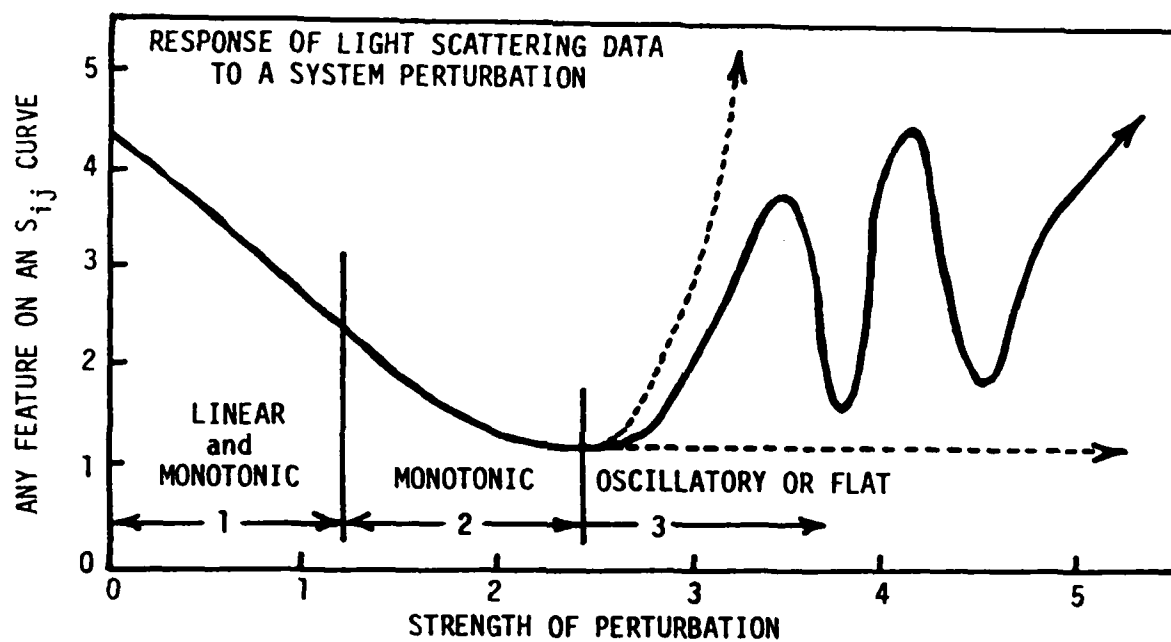
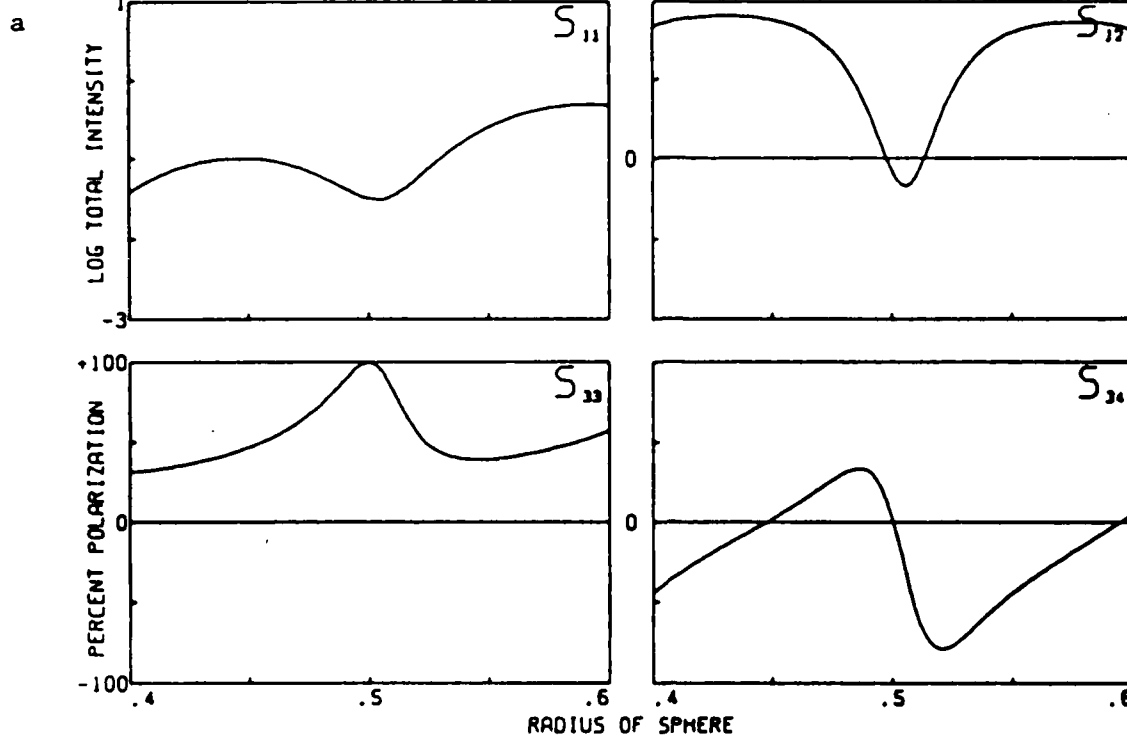


FIGURE 32. The Response of Light Scattering Data as a Function of System Perturbation

SPHERE SCATTERING AS A FUNCTION OF RADIUS OF SPHERE

REFRACTIVE INDEX OF MEDIUM= 1.000000
IMAGINARY REFRACTIVE INDEX= 0.000000
SCATTERING ANGLE= 90

REAL REFRACTIVE INDEX= 1.100000
WAVELENGTH= .441570



SPHERE SCATTERING AS A FUNCTION OF WAVELENGTH

REFRACTIVE INDEX OF MEDIUM= 1.000000
IMAGINARY REFRACTIVE INDEX= 0.000000
SCATTERING ANGLE= 90

REAL REFRACTIVE INDEX= 1.100000
RADIUS OF SPHERE= .600000

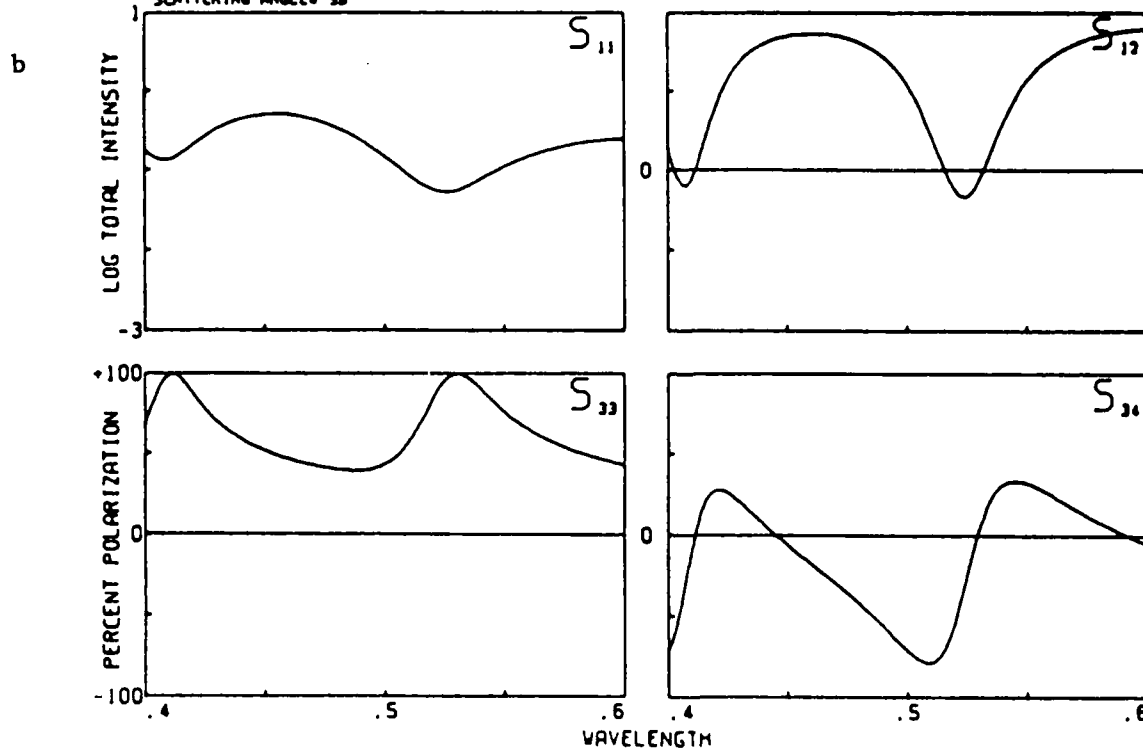
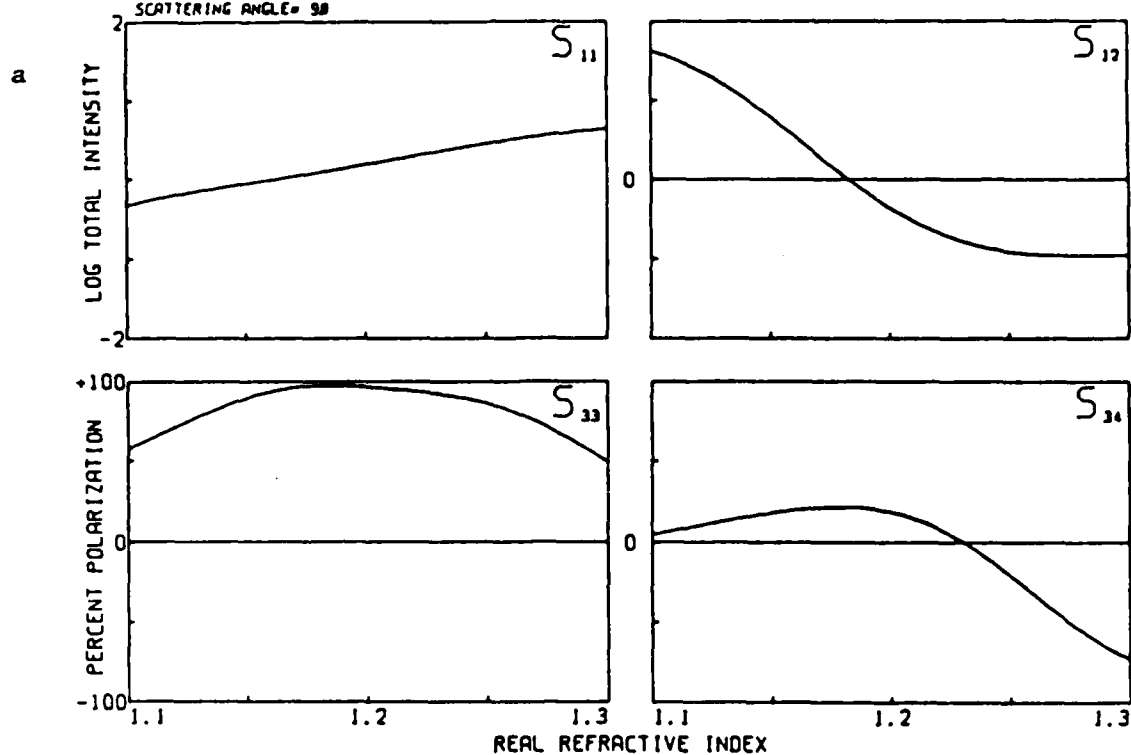


FIGURE 33. Response of Matrix Elements to a Change in Sphere Radius and Illuminating Wavelength

SPHERE SCATTERING AS A FUNCTION OF REAL REFRACTIVE INDEX

REFRACTIVE INDEX OF MEDIUM= 1.000000
RADIUS OF SPHERE= .600000
SCATTERING ANGLE= 90

IMAGINARY REFRACTIVE INDEX= 0.000000
WAVELENGTH= .441570



SPHERE SCATTERING AS A FUNCTION OF IMAGINARY REFRACTIVE INDEX

REFRACTIVE INDEX OF MEDIUM= 1.000000
RADIUS OF SPHERE= .600000
SCATTERING ANGLE= 90

REAL REFRACTIVE INDEX= 1.100000
WAVELENGTH= .441570

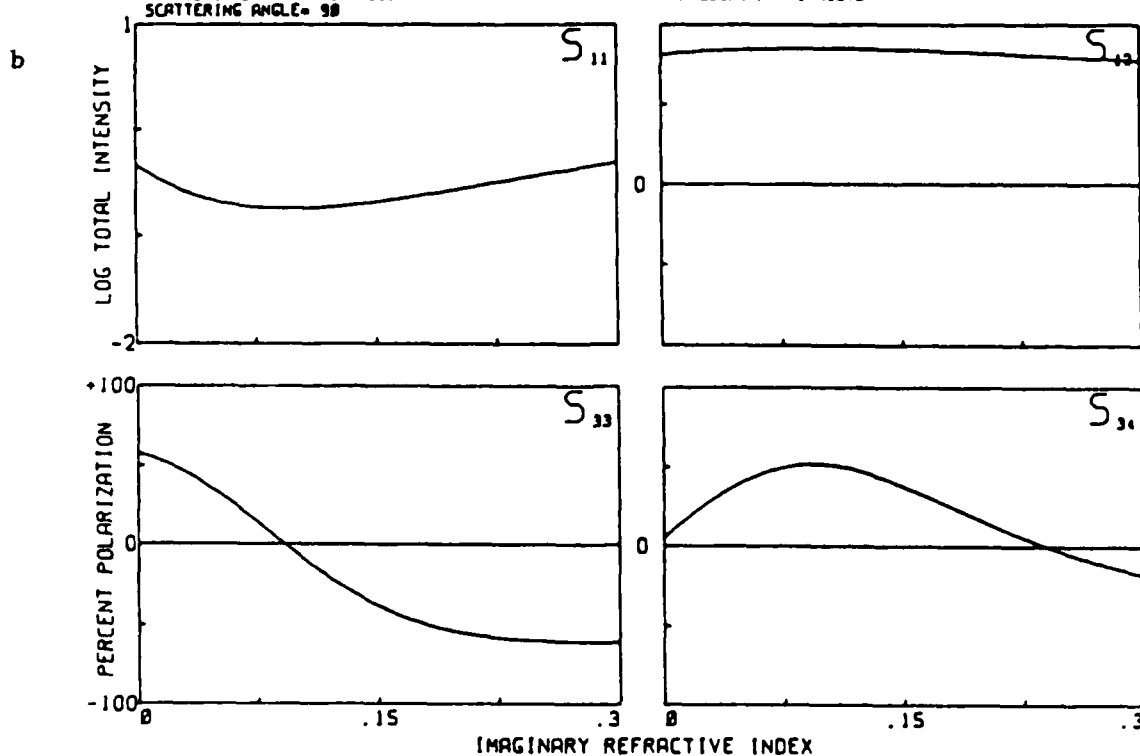


FIGURE 34. Response of Matrix Elements to a Change in Refractive Index and Absorption

radius change is similar to wavelength change except for a small change in the wavelength-dependent refractive index. Consequently, angle scans with fixed wavelength or wavelength scans with fixed angle give almost identical data and equal sensitivity to change. For this case, matrix elements S_{12} and S_{34} would be the first choices as probes since their signals go through zero polarization at some wavelength or radius. Matrix elements S_{12} and S_{33} , in contrast to S_{34} , have rather large regions of flat response making them insensitive as size indicators at certain sizes. However, placing the detector at another, more favorable angle can prevent this problem by adjusting the probe to lie in the steepest slope of the curves.

Figures 34a and b show the S_{ij} response at $\theta = 90^\circ$ as the real refractive index (n_1) changes from 1.1 to 1.3 and as the imaginary part (n_2) changes from 0.0 to 0.3. Although these curves are special cases described by the particle parameters listed above each figure, they show that the proper choice of matrix element (and scattering angle) can maximize the probe's effectiveness. For these cases S_{12} would be the least sensitive to an imaginary index change whereas it is the most sensitive to a real index change. Matrix element S_{34} is the second choice, giving respectable responses (and going through zero) over the entire range. S_{33} is too flat for an indicator of changes in n_1 , whereas it responds respectably to changes in n_2 .

These studies were also done for the forward and backward scatter, as well as at other "useful" angles. The main point is to show that light scattering can be a sensitive probe if, in advance, the response of various matrix elements is known over the range in which the perturbation is to occur. If an applied perturbation is expected to affect one of the parameters of a scattering system, both the choice of matrix element and scattering angle for a particular illuminating wavelength can be selected to maximize the probe's sensitivity. Showing that this can be done and that the information gained can be substantial is one of the main conclusions of this work.

2.8 Loss of Oscillatory Phase Information on Light Scattering Curves .

Polarized light scattering data from suspended particulates are often devoid of the important oscillatory phase information needed to accurately characterize the scattering system. The absence of phase information can be due to the properties of the one individual particle or of the many-particle system. We will examine the loss of phase information from perfect and imperfect particle systems by considering data from (1) very small Rayleigh particles, (2) very large Mie spheres, (3) polydispersed spheres, (4) highly absorbing spheres, (5) multiple scattering spheres, (6) Rayleigh-Gans spheres, and (7) irregular particles.

Figure 35 illustrates how phase information from large perfect spheres can be lost as the particles become irregular or mixed with different particles. As the particle systems in rows B, C, D, and E progress to the right, they become more complex, causing their light scattering curve, row A, to become less complex. It is because of this fact that light scattering data can be unreliable as a diagnostic tool. Our research has examined the polydispersive systems of perfect spherical particles (which are exactly solvable theoretically and attainable experimentally) and irregular particles--both of which give smooth light scattering curves.

When phase loss is severe, the light scattering data are not unique to the scattering interaction. Inversion will then yield wrong or highly

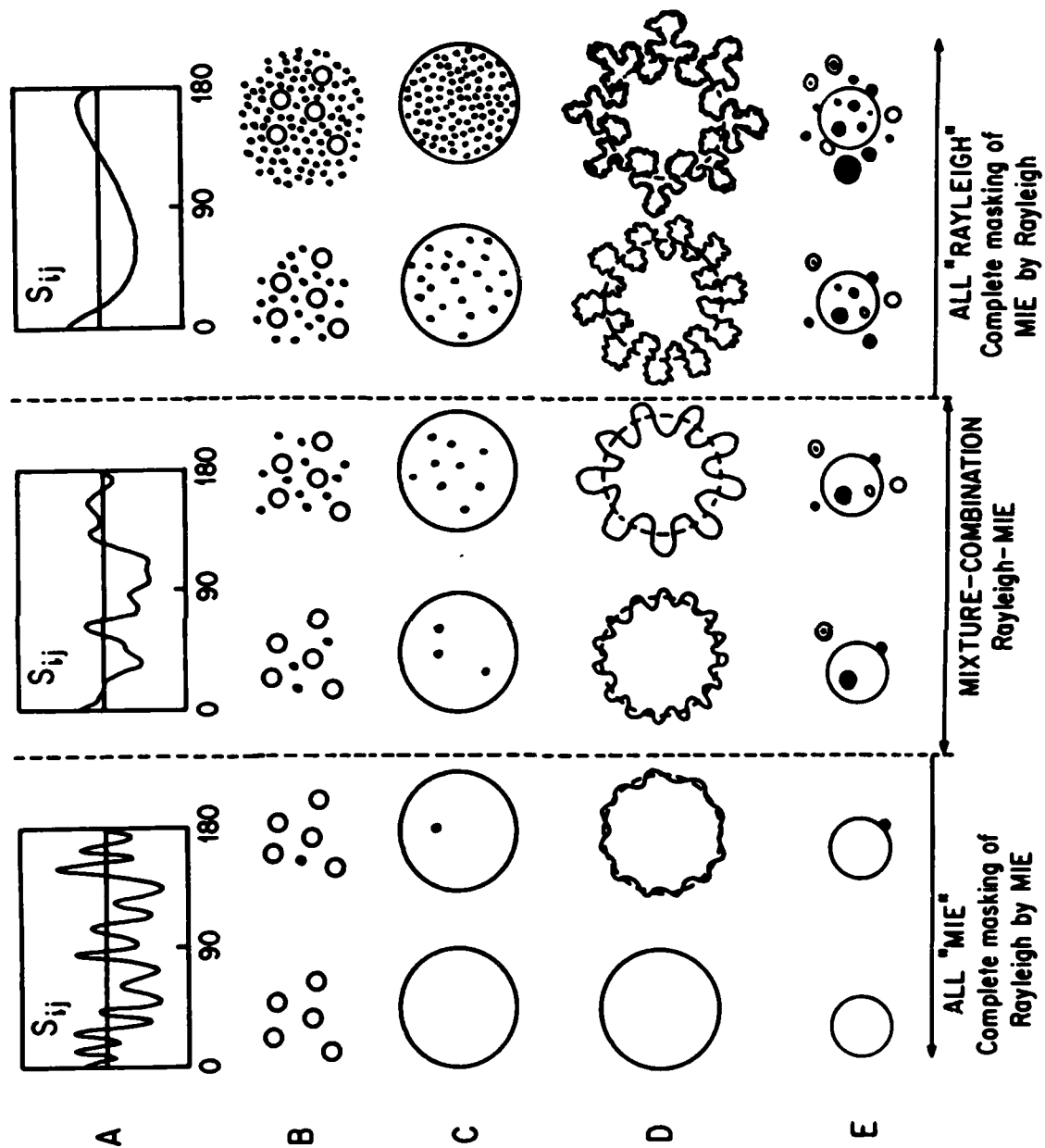


FIGURE 35. Expected Loss of S_{ij} Phase Information as a Function of Particle Irregularity

uncertain values for the optical and geometrical constants. In some cases, however, the remaining data are sufficient to partially characterize the scattering system.

2.8.1 Small Rayleigh Particles.

The simplest particle system for which the diffraction (scattering) of electromagnetic radiation can be calculated exactly is that of a small Rayleigh sphere (or any particle) whose diameter is much less than the wavelength of light. The well-known Rayleigh angular intensity distribution and the polarizations are displayed in Figure 36 in the context of the four nonzero light scattering matrix elements, S_{ij} for spheres. Matrix element S_{11} represents the θ -dependent scattered total intensity distribution, $I(\theta)$, which for a small particle is symmetrical about the slight intensity minimum at 90° . S_{11} corresponds exactly to the central maximum of the single slit diffraction pattern, where for a slit width $d = \lambda$, the first minimum ($m = 1$) would occur at $\theta = 90^\circ$. The matrix element S_{12} representing the θ -dependent linear polarization is equal to the function $\sin^2\theta$. The matrix element S_{33} representing the coupling of 45° linear polarization is equal to the function $\cos^2\theta$. The matrix element S_{34} measuring circular polarization is equal to zero, since Rayleigh particles (by definition) are too small to evoke any geometrical or optical path difference between any extreme rays that it scatters. All other matrix elements S_{ij} are zero.

We call attention to some important properties of the light scattering curves for Rayleigh particles. S_{11} and S_{12} are symmetric, while S_{33} is antisymmetric about $\theta = 90^\circ$. S_{34} is zero everywhere. In addition, the S_{ij} for spheres in general are characterized by other bounds: S_{12} and S_{34} are always zero at $\theta = 0^\circ$ and 90° . S_{33} is $+100\%$ at $\theta = 0$ and -100% at $\theta = 180^\circ$. These bounds hold regardless of how the S_{ij} curve may fluctuate between the end points at 0° and 180° . They are independent of the wavelength, particle size, refractive index, and absorption--so long as all particle properties are spherically distributed. This condition does not occur for single ellipses, fibers, and other irregular particles.

The four Rayleigh matrix element curves of Figure 36 represent the "starting point reference curves" for all light scattering curves from particulates. They form the baselines from which curves for larger particles grow and to which curves from complex systems might approach. These curves are independent of particle size, shape, and orientation for individual and collections of Rayleigh particles that scatter singly and independently. For non-independent and multiple scattering from even small particles, these curves will appear slightly distorted. It is proper to consider that the Rayleigh curves contain no phase information. The desired oscillatory phase information, which is truly indicative of larger particles and responsive to particle size changes, appears on these curves only for larger particles. This is discussed in the next section.

2.8.2 Large Mie Spheres.

As the size of the Rayleigh sphere increases, all the S_{ij} become distorted and begin to show phase information indicative of larger particles.

Figure 37 shows the four nonzero S_{ij} for an $r = 0.15$ micron particle, for a particle 1% larger (solid lines), and their difference (dotted line). The new information, indicating scattering by a larger particle (of the order of

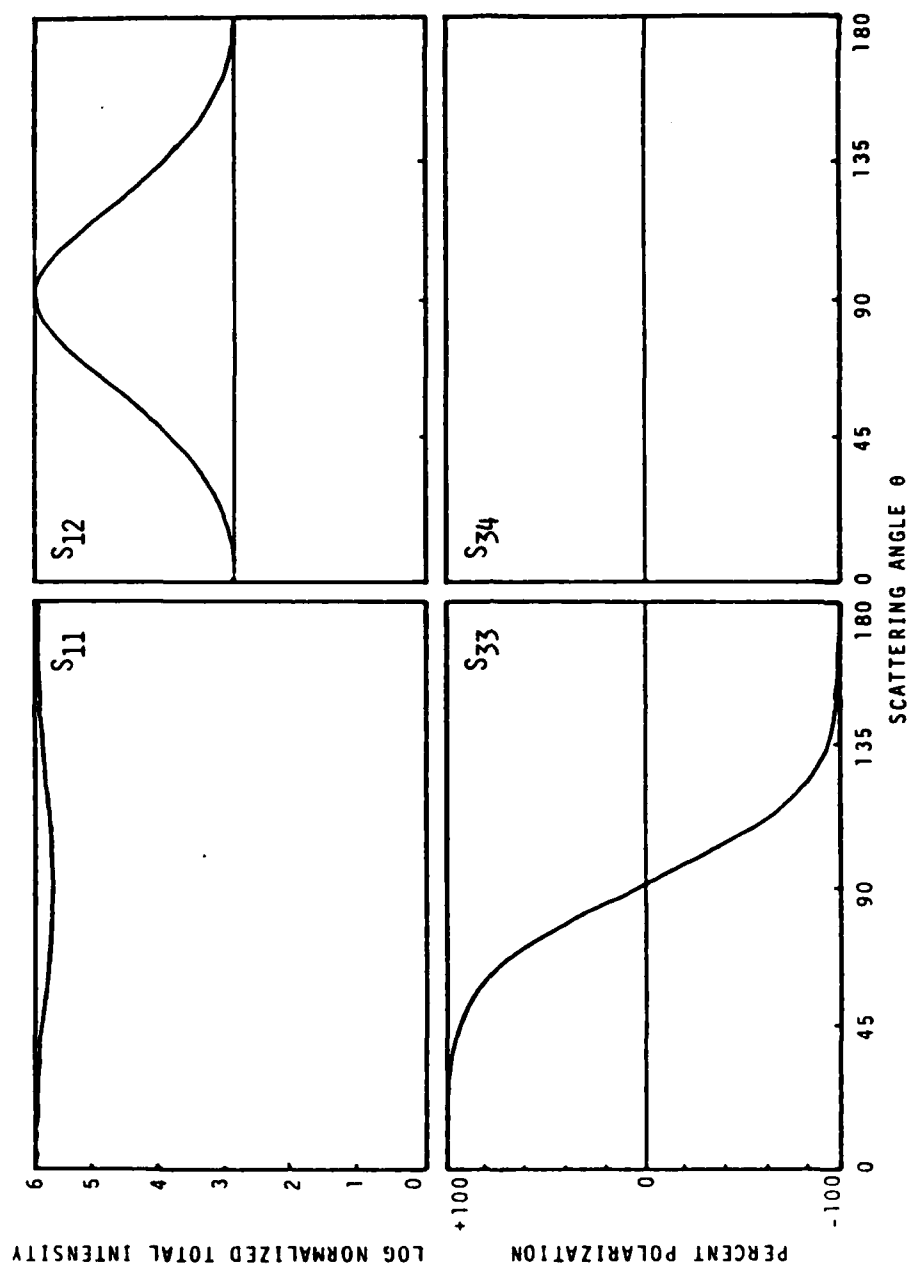


FIGURE 36. Matrix Elements for Rayleigh Spheres

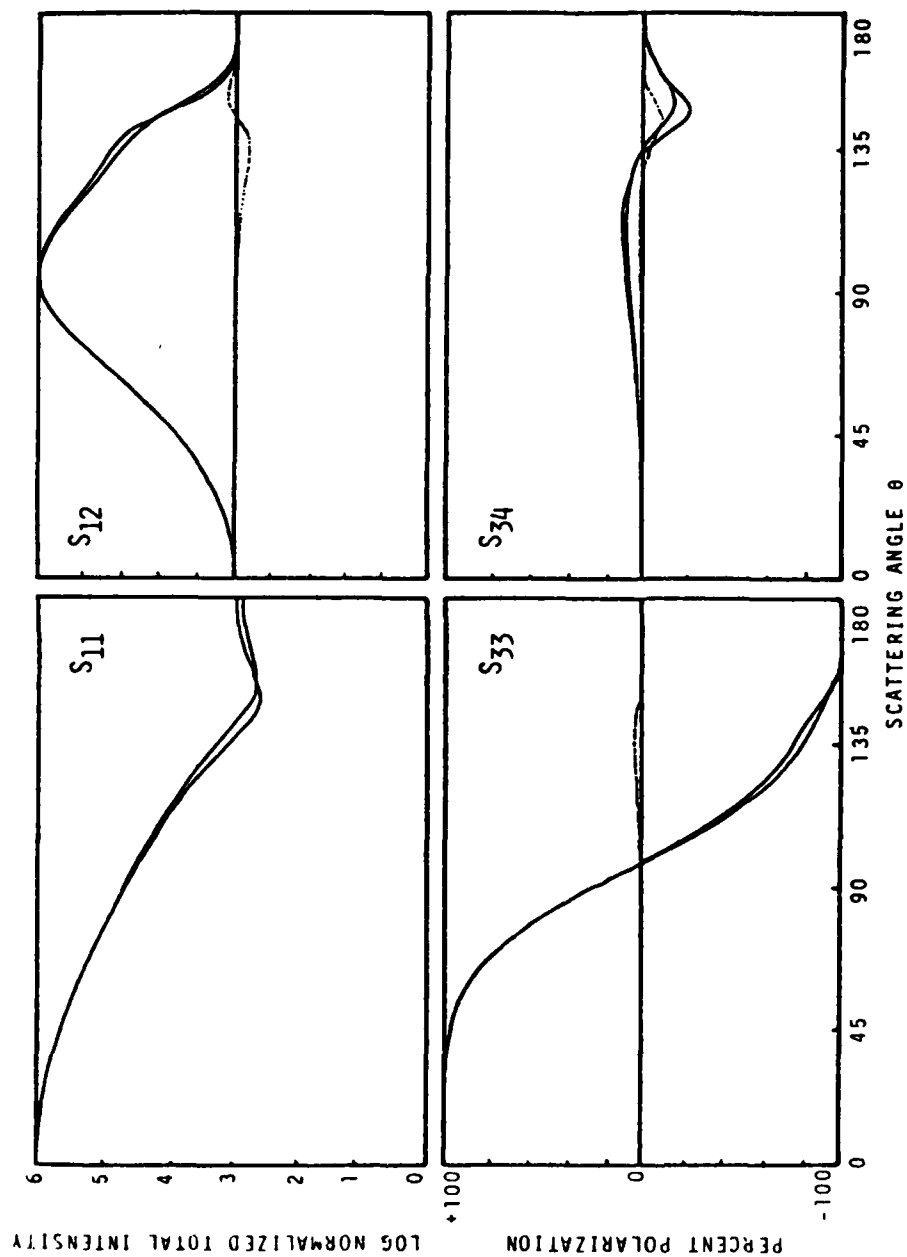


FIGURE 37. Matrix Elements for an $r = 0.15$ Micron Sphere and for a Sphere 1 Percent Larger

the wavelength) first occurs in the backscatter. Since this sphere is only slightly larger than Rayleigh, the distortion in the backscatter is the first oscillation. Note that the $r = 0.15$ micron sphere is about two-thirds the wavelength of the 0.4416 micron scattered radiation.

Figure 38 shows the same four matrix elements S_{ij} for an $d = 1.2$ micron sphere, for a sphere 1% larger (solid lines) and their difference (dotted line). Comparison of Figures 37 and 38 shows that a small (1%) change in size of a large particle contributes a more significant change to the scattering data than does the same percentage change in a small particle. Consequently, a small amount of polydispersivity in a collection of large particles will destroy backscatter phase information for larger particles much more than for smaller. Size polydispersivity is the main destroyer of phase information on light scattering curves from large particles.

2.8.3 Polydispersed Spheres.

Figure 39 shows the four S_{ij} for a polydispersed sphere system with equal numbers of monodispersed particles of size = 0.52, 0.54, 0.56, 0.58, 0.60, 0.62, 0.64, 0.66, and 0.68 microns. The average size is 0.60 microns. As expected, the backscatter suffers the largest loss of phase information, although there is general loss everywhere. Its absence can cause large uncertainties in the particle size determinations.

An interesting question concerns the shape of the S_{ij} curves for systems that are totally polydispersive in size (and all other properties). The first guess that all S_{ij} (except S_{11}) would be zero is wrong. Experimental work and computer modeling show that they "tend toward" the Rayleigh curves shown in Figure 36. Although the S_{ij} are smoother and tend toward the Rayleigh limit, phase destruction is not complete. Generally S_{34} remains nonzero. The other S_{ij} , although almost smooth, are not symmetric about 90° and show reduced polarization.

2.8.4 Absorbing Fibers.

Increasing the absorption of perfect spheres and fibers destroys virtually all phase information in the backscatter direction. Figure 40 shows the matrix element S_{11} as a function of absorption for an $R = 1.0$ micron fiber system. Although most of the phase information is gone, the more than one order of magnitude decrease in backscatter (compared to forward scatter) is still indicative of large particles. The phase information remaining in the forward scatter ($<60^\circ$) gives a very accurate value for the diameter of the sphere from aperture diffraction theory. This calculation is quite valid for highly absorbing fibers, since light scattering dominated by high absorption is almost independent of the refractive index. The absorbing fiber is essentially the complement of a clear aperture in an opaque plate. Therefore their scattering should be similar, as suggested by Babinet's principle. The essentially flat backscatter ($>90^\circ$) prevents this system from being confused with low index particles slightly larger than Rayleigh.

2.8.5 Multiple Scattering Spheres.

Figure 41 shows the progressive loss of phase information on S_{ij} in response to increased multiple scattering by spheres. Each adjacent curve represents a factor-of-2 difference in concentration of 0.80 micron spheres. All S_{ij} lose phase information and become smooth with increased multiple

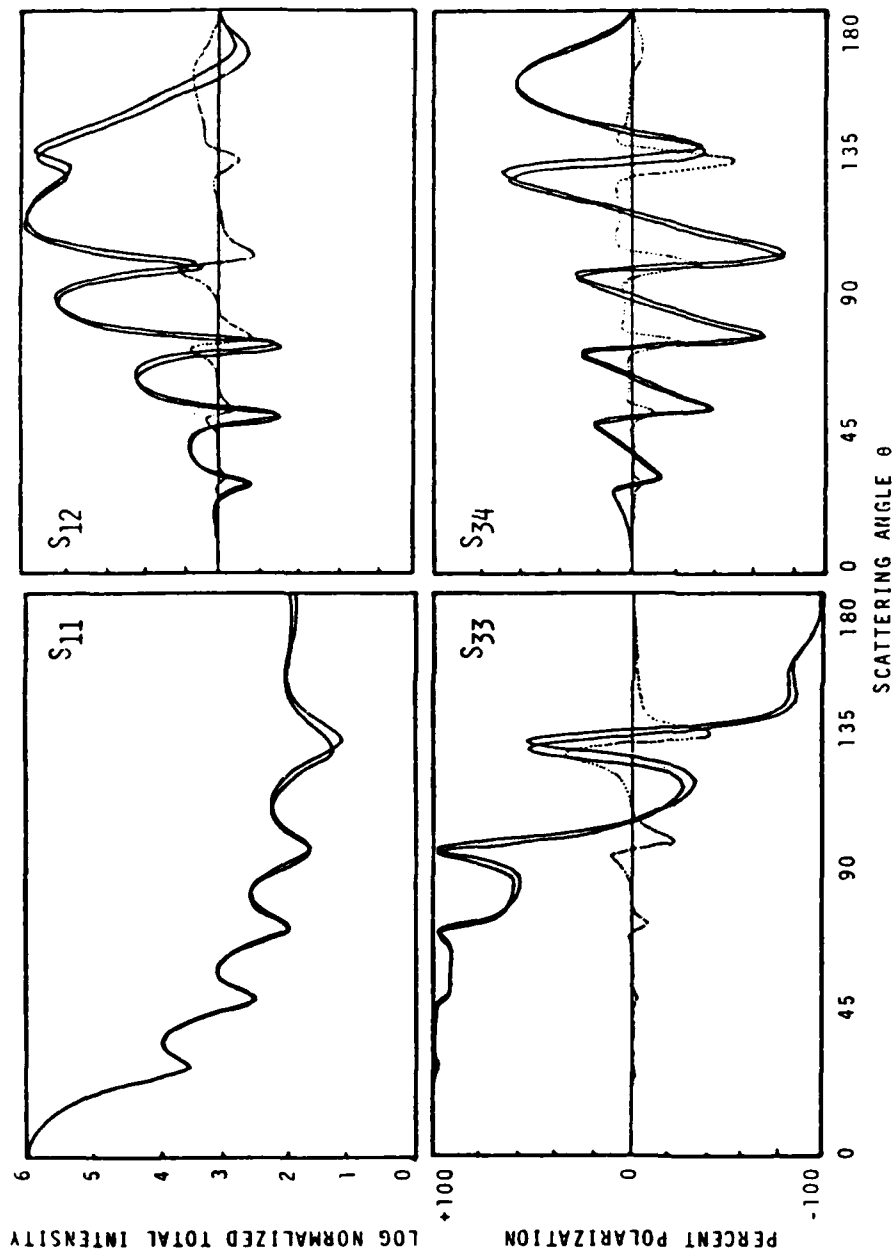


FIGURE 38. Matrix Elements for an $r = 0.6$ Micron Sphere and for a Sphere 1 Percent Larger

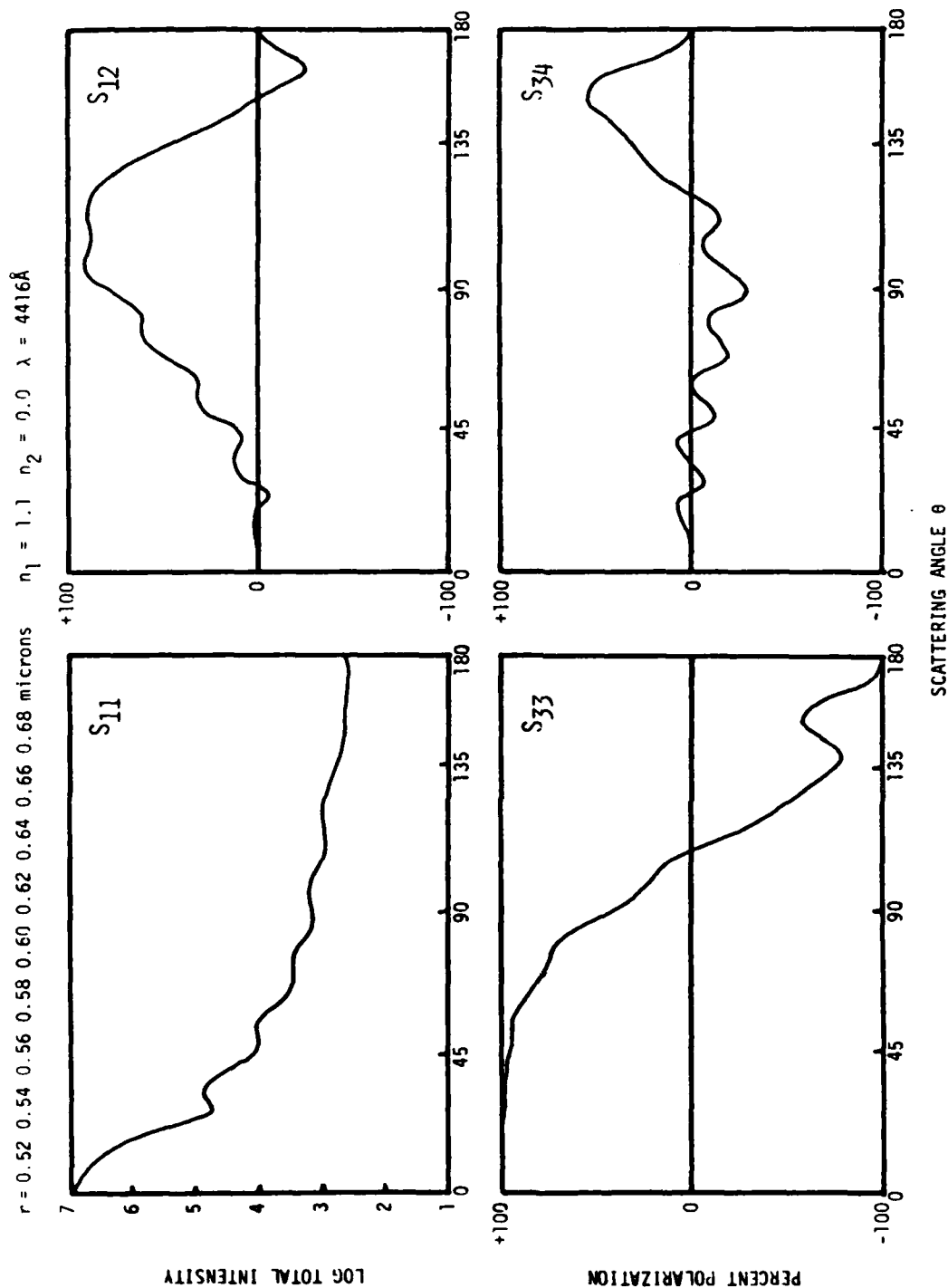


FIGURE 39. Matrix Elements for a Nine-Component Sphere System

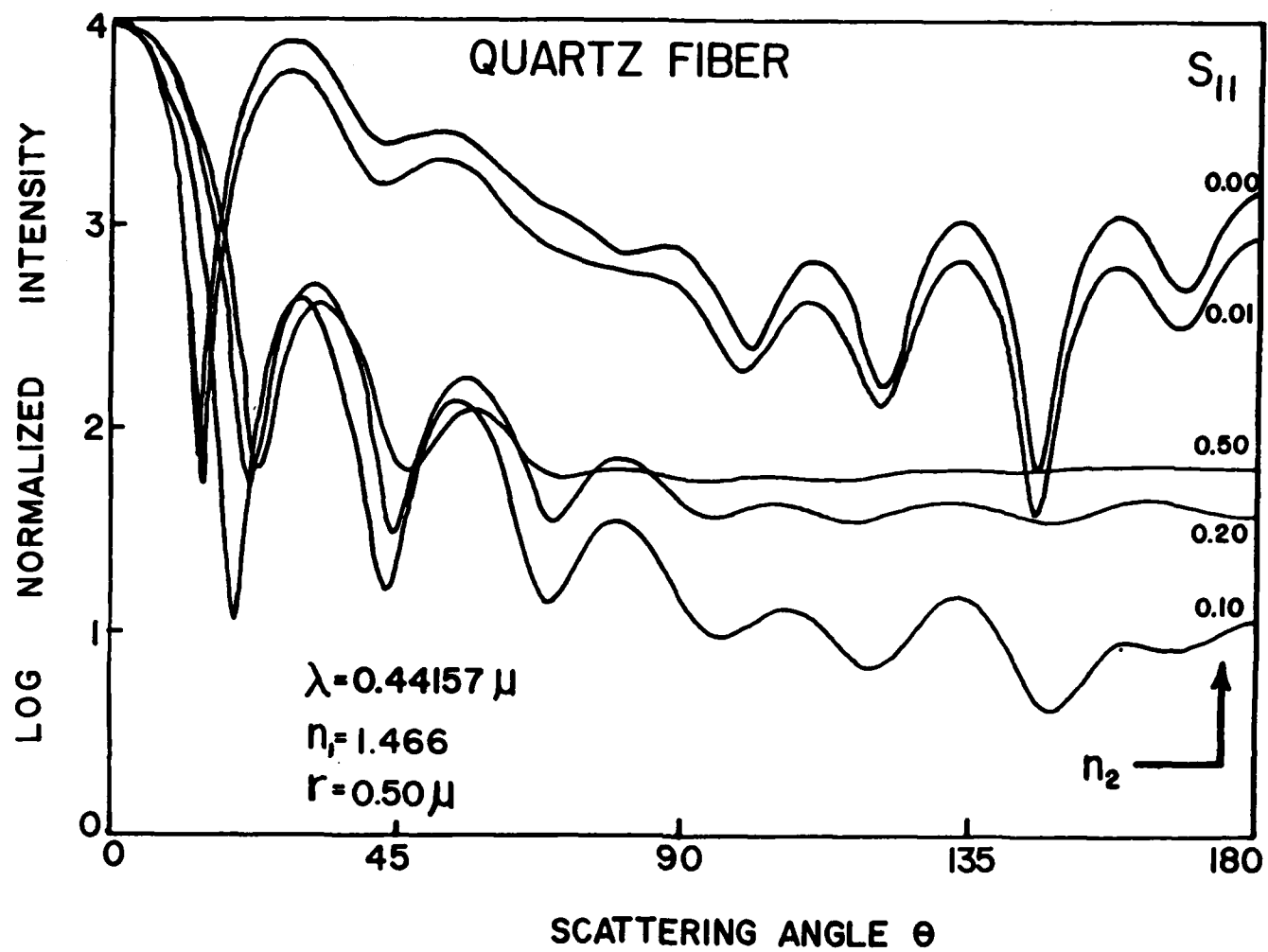


FIGURE 40. Matrix Element S_{11} as a Function of Absorption

LIGHT SCATTERING FROM MULTIPLE SCATTERING SPHERES

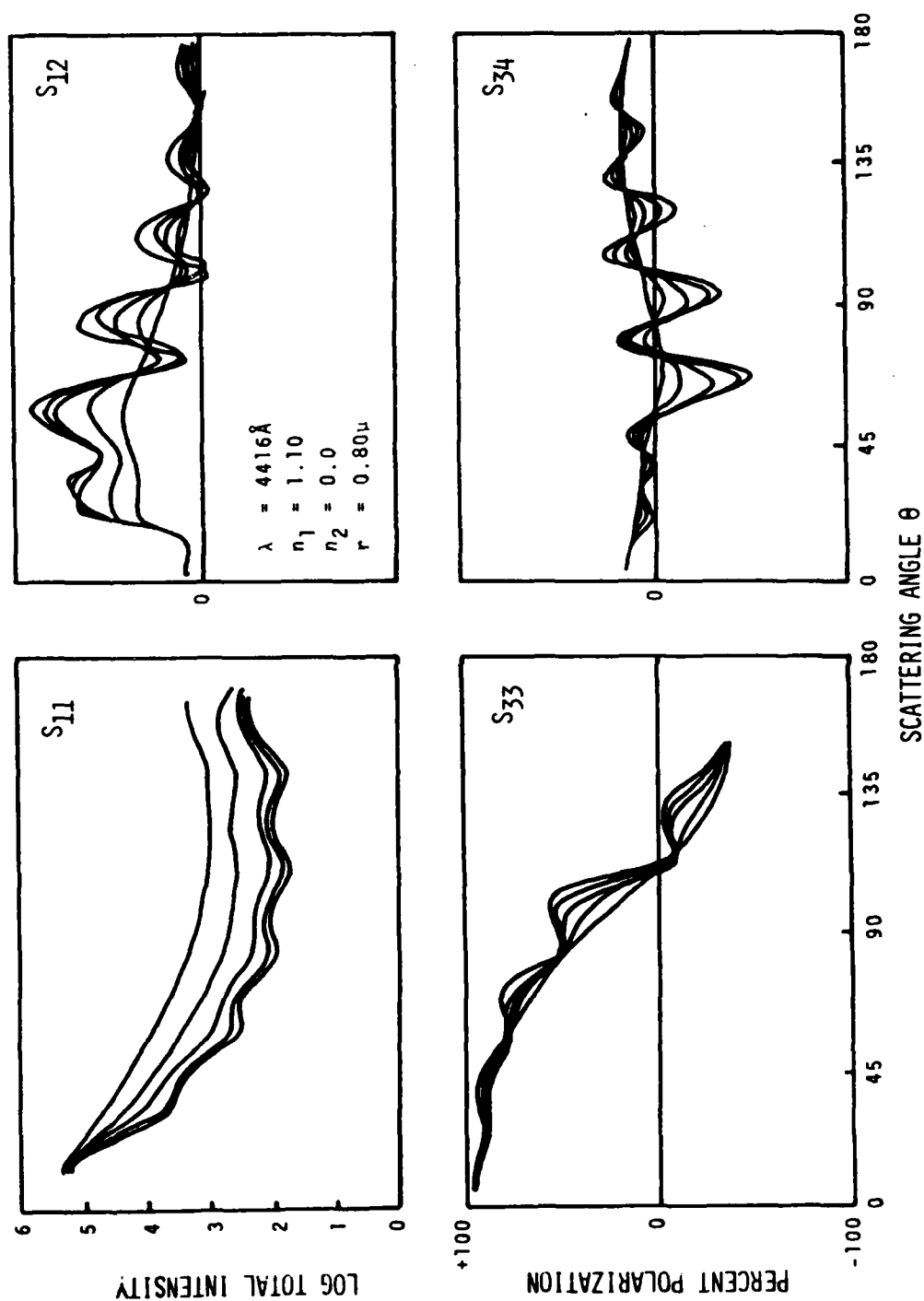


FIGURE 41. Matrix Elements from a Multiple Scattering Sphere System as a Function of Concentration

scattering. S_{33} is quite similar to the Rayleigh sphere signal except for a small shift of the 90° zero polarization crossing point to higher angles. In this multiple scattering system, S_{12} and S_{34} tend to oscillate about the final smooth curve while S_{33} approaches it tangentially. Evidently, extreme multiple scattering does not create Rayleigh shape signals in the limit. In this case, S_{12} is driven away from the Rayleigh limit while S_{33} oscillates about its nonzero highly multiple scattering limit.

2.8.6 Irregular Particles.

Figure 42 shows the four matrix element signals for Arizona road dust. This is a log-normal system of irregular particles polydispersed in all optical and geometrical constants. A scanning electron micrograph of the particle system is shown in Figure 43. All matrix elements are smooth. Matrix elements S_{12} and S_{33} appear almost Rayleigh except that the minimum of S_{12} and the zero crossing point of S_{33} are shifted approximately 20° toward the backscatter. S_{34} is almost zero as it is for Rayleigh spheres. S_{11} , varying by more than 2.5 orders of magnitude and increasing in the backscatter, is the only signal that suggests that the particles are large with high refractive index and low absorption.

These six examples show that oscillatory phase information can be missing or destroyed in light scattering data for many reasons. Consequently, certain conclusions about scatterers giving smooth light scattering curves must be carefully drawn and qualified. Studies are underway to determine the accuracy of the optical and geometrical constants extracted from data with minimal phase information. These studies show that in general, light scattering measurements do not give accurate values for the optical, electrical, or geometrical constants of particulates.

Although conclusions are often very system dependent, we can draw a few important ones that seem to characterize a large class of light scattering curves.

- a. Smooth curves do not imply small Rayleigh particles.
- b. Size polydispersivity is the main destroyer of phase information from perfect sphere systems.
- c. Polydispersivity in the refractive index n_1 destroys phase information from perfect sphere systems.
- d. Absorption destroys phase information mainly in the backscatter, both for single spheres and particle systems.
- e. Particles that scatter approximately equal intensity in the forward and backscatter are either Rayleigh (small) or large polydispersed systems with a high refractive index and zero (or very low) absorption.
- f. A total intensity signal S_{11} , symmetric about its few percent intensity dip at 90° is from a Rayleigh system.
- g. Low index, large particles (approximate Rayleigh-Gans systems) scatter much less in backscatter than in forward scatter.

LIGHT SCATTERING FROM POLYDISPERSED ARIZONA ROAD DUST

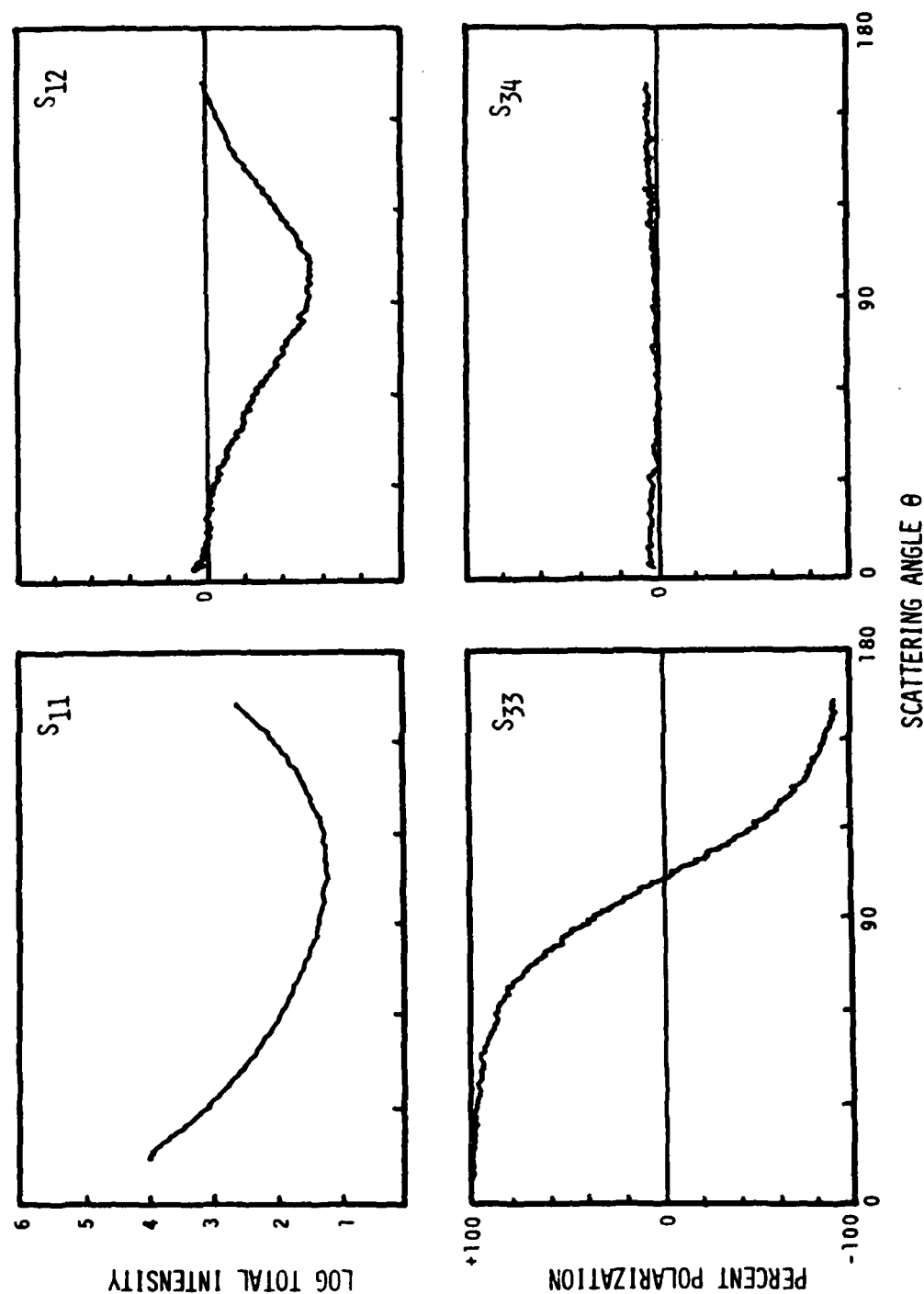


FIGURE 42. Matrix Elements from Arizona Road Dust, a Polydispersed Irregular Particle System

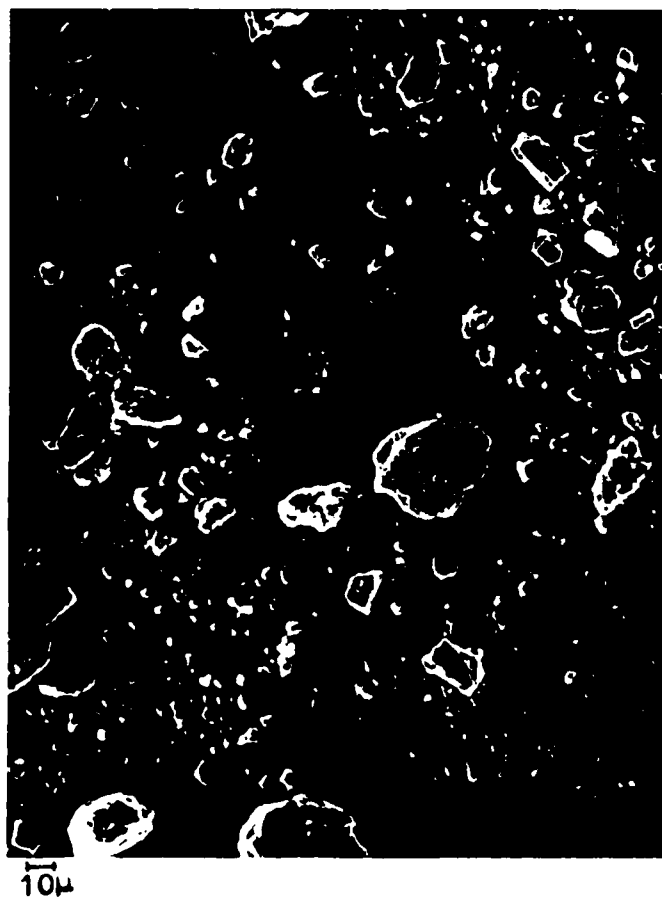


FIGURE 43. Electron Micrograph of Arizona Road Dust

These conclusions, if applied carefully, should be helpful in extracting some general but useful information about a scattering system. These results show that if only one matrix element curve is available or if information is gathered over a limited angular range, the information extracted will definitely be limited.

3. CONCLUSIONS

The experimental work carried out over the past 2 years with Army support is finished, and the major results have been reported in this final report. As with any good research, new questions have been asked and other paths of investigation have opened up. Therefore, the techniques we developed and the results we report will affect our ongoing research program for years to come. Some unanswered questions and new applications will be pursued during the next 2 years with Army funding, some others will be supported by other grants.

A number of papers are in preparation for publication in the referenced journals. Several topics reported in the results will be written as separate papers. In addition to the progress reports, and this final report, many results have been reported at seminars and colloquia in various departments throughout the University--chemistry, optical sciences, lunar and planetary sciences, geosciences, microbiology, etc.--wherever light scattering techniques are used to extract data. Researchers in those departments have benefitted greatly from our work on complex particles, since most of their scatterers are irregular. The techniques developed in these experiments are now being extended to surfaces under a continuing Army grant from CRDC. It is interesting to see how these ideas were developed and extended: from a sphere = point; to a fiber = line; to a surface = area. We are optimistic that the Mueller Matrix-Stokes Vector approach to light scattered from surfaces will also be a valuable contribution to fundamental science and technology.

END

FILMED

9-85

DTIC